

1 **Novel insights into deep groundwater exploration by geophysical estimation of**
2 **hard rock permeability**

3 **Muhammad Hasan**^{1,2,3,*}, **Lijun Su**^{1,2,3,**}

4 ¹ *State Key Laboratory of Mountain Hazards and Engineering Resilience, Institute of Mountain*
5 *Hazards and Environment, Chinese Academy of Sciences, Chengdu 610299, China*

6 ² *China-Pakistan Joint Research Center on Earth Sciences, CAS-HEC, Islamabad, Pakistan*

7 ³ *University of Chinese Academy of Sciences, Beijing 100049, China*

8

9 *Corresponding authors:

10 Muhammad Hasan: Email: mhasan@imde.ac.cn; ORCID: [https://orcid.org/0000-0001-6804-](https://orcid.org/0000-0001-6804-7962)
11 7962; Phone Number: +86-13051361710

12 Lijun Su: Email: sulijun1976@163.com; ORCID: <https://orcid.org/0000-0001-9972-4698>

13 Corresponding authors' postal address: State Key Laboratory of Mountain Hazards and
14 Engineering Resilience, Institute of Mountain Hazards and Environment, Chinese Academy of
15 Sciences, Chengdu 610299, China

16

17

18

19

20

21

22

23 **Abstract**

24 Deep groundwater exploration in hard rock terrains is critical in regions where deep aquifers may
25 offer long-term water security amidst an increasing scarcity. However, such exploration is
26 globally challenged by geological complexity and the limitations of traditional investigative
27 techniques. Accurate estimation of hydraulic parameters, particularly permeability (k), is
28 essential for effective groundwater management and future resource planning. Conventional
29 borehole-based methods for measuring k are invasive, costly, time-consuming, and limited to
30 sparse, point-scale observations, making them inadequate for characterizing deep and
31 heterogeneous aquifer systems. Geophysical methods offer a promising non-invasive alternative,
32 enabling broader spatial coverage with reduced surface disturbance. Previous empirical
33 geophysical approaches, such as vertical electrical sounding (VES), are generally restricted to
34 shallow depths (<200 m), relatively homogeneous geological settings, and one-dimensional
35 interpretations. This study demonstrates, for the first time, the use of controlled-source audio-
36 frequency magnetotellurics (CSAMT) to estimate two- and three-dimensional k distributions to
37 depths exceeding 1 km in crystalline and sedimentary terrains. The method relies on an empirical
38 resistivity–permeability relationship calibrated using 116 core samples from six boreholes (0–
39 200 m). While the specific equation derived in this study is site-specific to the Jinji area and
40 should not be directly transferred elsewhere, the broader methodology, integrating CSAMT
41 resistivity with local borehole calibration, offers a transferable framework for k estimation in
42 other complex geological settings. The results show that CSAMT, when calibrated with borehole
43 data, can reliably capture deep subsurface variability and produce spatially continuous
44 hydrogeological models in hard rock terrains. While CSAMT inversion is inherently ill-posed,
45 the incorporation of ground-truth data significantly enhances model robustness and

46 interpretability. By reducing dependence on extensive drilling, this approach represents a
47 significant advancement in deep groundwater exploration. It provides a scalable methodology for
48 sustainable groundwater resource management, while emphasizing the need for local calibration
49 in any new application.

50 **Keywords:** Permeability; Geophysical methods; Hydraulic parameters; Groundwater; Hard rock;
51 Hydrogeological models

52 **1 Introduction**

53 Metamorphic and igneous rocks dominate Earth's crust and cover about one-third of its surface
54 (Amiotte Suchet et al., 2003). In hard rock terrains, groundwater research focuses on delineating
55 subsurface structures, such as faults and fractures that control water storage and flow (Fernando
56 and Pacheco, 2015; Hasan et al., 2021). A key parameter in this context is aquifer potential,
57 which reflects the capacity of rock formations to store and transmit groundwater and is
58 influenced by lithology, structural complexity, mineral composition, weathering, and infiltration
59 depth (Majumdar and Das, 2011; Zhu et al., 2017). However, accurately characterizing the
60 lateral and vertical heterogeneity of these properties remains challenging due to limited data and
61 the complexity of massive rock units (Dewandel et al., 2006). In such settings, conventional
62 methods often fall short, leading to inefficient or unsustainable groundwater development
63 (Nwosu et al., 2013; Worthington et al., 2016). Developing cost-effective and reliable
64 approaches for subsurface assessment is therefore essential for managing groundwater in hard
65 rock environments.

66 Groundwater at depths beyond 500 m is typically isolated from surface hydrological
67 influences and often exhibits brackish or saline characteristics (Ferguson et al., 2023). Its

68 strategic importance is increasingly recognized, particularly in geologically- and
69 environmentally-constrained settings (Gleeson et al., 2014). In the Jinji region, several factors
70 necessitate focused investigation of deep aquifers. Surface water is scarce and unreliable, while
71 the shallow subsurface is dominated by fresh granite, which has inherently low porosity and
72 permeability, limiting groundwater availability. By contrast, deeper fractured zones in granite,
73 sandstone, and hornstone present more favorable hydrogeological conditions. Recent national
74 water initiatives in China have emphasized deep subsurface exploration in structurally complex
75 terrains to identify underutilized aquifers for enhancing long-term water security.
76 Comprehensive assessment of these deep reserves is essential to evaluate their recharge potential
77 and integrate them into sustainable resource management strategies (Condon et al., 2020; Hasan
78 and Shang, 2022). As pressure on surface and shallow groundwater intensifies, deep aquifers
79 may serve as a vital buffer against increasing environmental and socio-economic stress.

80 Multiple studies have documented the rapid depletion of global groundwater reserves,
81 raising serious concerns about long-term water sustainability (Wada et al., 2010; Laghari et al.,
82 2012; Jasechko et al., 2024). Addressing this challenge requires accurate and detailed
83 assessments of groundwater resources, which depend critically on a clear understanding of
84 subsurface hydraulic properties. Permeability (k) is a key parameter that describes the ease with
85 which fluids can move through a porous medium, while the capacity to store water is more
86 directly characterized by porosity. This parameter is crucial for aquifer analysis in various
87 hydrogeological settings (Allègre et al., 2016; Esmaeilpour et al., 2023; Carbillet et al., 2024).
88 Borehole testing remains the standard method for estimating k and related aquifer parameters
89 (De Lima and Niwas, 2000; Hasan et al., 2021). However, borehole investigations are often
90 limited by high costs, logistical challenges, and poor spatial coverage, particularly in rugged

91 terrains, while offering only localized information with limited ability to image lateral and deep
92 structures (Singh, 2005; Fiandaca et al., 2018). These limitations contribute to uncertainties in
93 groundwater assessments, especially in data-scarce regions (Hasan and Shang, 2022).
94 Alternatively, it is essential to develop methods that minimize reliance on costly drilling while
95 still enabling reliable estimation of permeability within prospective rock formations.

96 Geophysical methods are widely and effectively employed to enhance subsurface
97 characterization in groundwater studies (Daily et al., 1992; Jardani et al., 2007; Hinnell et al.,
98 2010; Fu et al., 2013; Jiang et al., 2014; Kouadio et al., 2023). Compared to conventional
99 drilling, these techniques offer significant advantages in cost, deployment speed, environmental
100 impact, and spatial extent (Hu et al., 2013; Fusheng et al., 2022). Their ability to image
101 subsurface variations in both vertical and lateral dimensions makes them particularly effective in
102 heterogeneous terrains (Hasan et al., 2025). Among them, resistivity-based methods are widely
103 used due to their sensitivity to lithology, porosity, fractures, and fluid content (Hasan et al., 2021;
104 Asfahani, 2023). Common techniques include electrical resistivity tomography (ERT), vertical
105 electrical sounding (VES), and electromagnetic methods such as magnetotellurics (MT), time-
106 domain electromagnetics (TDEM), and controlled-source audio-frequency magnetotellurics
107 (CSAMT) (Soupios et al., 2007; Bauer-Gottwein et al., 2010; Pollock and Cirpka, 2012; Jiang et
108 al., 2014; Di et al., 2020). A comparative summary of these methods (Table 1) highlights their
109 relative strengths and limitations in terms of depth penetration, spatial resolution, sensitivity to
110 cultural noise, and cost. VES is cost-effective but limited to shallow one-dimensional profiling
111 (<200 m) (Niwas and De Lima, 2003; Majumdar and Das, 2011). ERT improves resolution and
112 enables 2D/3D imaging up to ~300 m but requires intensive fieldwork and is less effective in
113 extreme resistivity environments (Abbas et al., 2022; Hasan and Shang, 2022). For deeper

114 targets, electromagnetic methods such as TDEM, MT, and CSAMT are often employed (Bauer-
115 Gottwein et al., 2010; Di et al., 2020; Gonzalez-Duque et al., 2024). MT achieves the greatest
116 depth penetration (up to tens of kilometers) but often sacrifices resolution in the upper crust and
117 is highly susceptible to cultural noise (Simpson and Bahr, 2005). TDEM provides rapid
118 deployment and intermediate depth coverage (hundreds of meters) but suffers reduced sensitivity
119 in resistive hard rock (Bauer-Gottwein et al., 2010). By contrast, CSAMT bridges these
120 approaches: with a controlled source and frequency tuning, it achieves intermediate-to-deep
121 penetration (>1000 m) with improved resolution in resistive hard rock settings and strong
122 immunity to cultural noise (Smith and Booker, 1991; Zonge and Hughes, 1991; Wang et al.,
123 2015; Zhang et al., 2021). The choice between resistivity and electromagnetic techniques is
124 contingent upon parameters like investigation depth, resolution requirements, geological
125 complexity, and logistical constraints (Majumdar and Das, 2011; Hasan et al., 2025). Given the
126 objectives of this study, to characterize deep fractured aquifers in crystalline and sedimentary
127 rocks under complex geological conditions, CSAMT was selected as the most suitable technique.
128 Its combination of depth penetration, resolution, and robustness against noise provides a practical
129 balance between regional coverage and site-specific imaging, enabling the development of 2D
130 and 3D permeability models that are otherwise difficult to achieve with alternative methods.

131 In fractured rocks like granite, metamorphic, and sandstone formations, fluid flow is
132 largely controlled by fracture networks rather than matrix porosity. Accurate hydraulic
133 assessment in such settings benefits from integrated geophysical and hydrogeological approaches
134 to better capture spatial variability and improve flow modeling (Hasan et al., 2021; Abbas et al.,
135 2022). Resistivity-based techniques are particularly valuable for delineating subsurface structures
136 and identifying water-bearing zones. Because electrical resistivity is sensitive to porosity,

137 saturation, fracture density, and fluid salinity, it is increasingly used to infer k in heterogeneous
138 geological settings (Mudunuru et al., 2022; Yan et al., 2024). Permeability is influenced by
139 numerous parameters, including porosity, fracture density and orientation, grain size distribution,
140 degree of weathering, pore connectivity, and saturation level, highlighting the utility of
141 resistivity measurements as indicators for evaluating groundwater flow potential (Gerke et al.,
142 2011; Worthington et al., 2016; Pellet et al., 2024).

143 Empirical and semi-empirical models have been developed to estimate hydraulic
144 properties from geophysical measurements, particularly in data-sparse regions (Niwas and De
145 Lima, 2003; Singh, 2005; Soupios et al., 2007; Hasan et al., 2021; Asfahani, 2023). In parallel,
146 resistivity-based methods and hydrogeophysical inversion techniques have been developed to
147 more rigorously estimate hydraulic parameters by integrating petrophysical relationships within
148 geophysical modeling frameworks (Daily et al., 1992; Ferré et al., 2009; Binley et al., 2010;
149 Hinnell et al., 2010; Herckenrath et al., 2012; Pollock and Cirpka, 2012; Herckenrath et al.,
150 2013; Binley et al., 2015). These approaches have improved resolution in parameter estimation,
151 particularly in shallow, unconsolidated, or relatively homogeneous settings. However,
152 applications to deep, fractured, and lithologically complex environments remain limited,
153 especially in terms of producing volumetric k models at kilometer-scale depths. Despite these
154 advances, generation of detailed 2D and 3D k maps from resistivity data in deep, hard-rock
155 terrains is constrained by limited borehole control, significant geological heterogeneity, and the
156 ill-posed nature of geophysical inversion. In such contexts, integrating resistivity data with
157 borehole measurements presents a practical, cost-effective solution for characterizing aquifer
158 properties over large areas and depth ranges. This study builds on prior hydrogeophysical
159 research by introducing a novel application of the CSAMT method for volumetric k modeling in

160 a complex, fractured hard-rock setting. While previous studies have applied resistivity-based
161 techniques to estimate hydraulic properties, this is the first to utilize CSAMT for constructing the
162 detailed 2D and 3D k modeling beyond 1000 m depth in geologically heterogeneous terrains
163 comprising hornstone, granite, and sandstone. Few available drilling tests were used to calibrate
164 CSAMT-derived resistivity with laboratory-measured k , allowing the resulting empirical
165 relationship to be applied across the broader survey domain. Several CSAMT profiles were
166 conducted along and beyond the borehole locations, and the calibrated resistivity–permeability
167 correlation was used to generate spatially continuous subsurface models in regions lacking direct
168 borehole data. This integration resulted in a robust, data-constrained workflow capable of
169 revealing k variations across diverse rock units and lithological boundaries. The method offers a
170 practical and scalable alternative to extensive drilling campaigns, enabling a more detailed and
171 cost-efficient evaluation of deep groundwater potential in structurally complex terrains.

172 Ultimately, this work extends the scope of hydrogeophysical methods by demonstrating
173 the feasibility of applying CSAMT for deep hydraulic parameter estimation in hard rock. It
174 bridges a critical methodological gap in hard-rock hydrogeology and sets the foundation for
175 future CSAMT-based volumetric modeling in similarly challenging environments. This study
176 aims to develop and apply a geophysical-based approach for mapping the spatial distribution of k
177 in deep, hard-rock settings. By integrating CSAMT data with targeted borehole measurements,
178 this research enhances 2D and 3D hydrogeological assessments across heterogeneous lithologies
179 in structurally complex terrains. It also minimizes reliance on extensive drilling, demonstrating
180 the value of non-invasive geophysical techniques as a cost-effective alternative for deep
181 groundwater exploration.

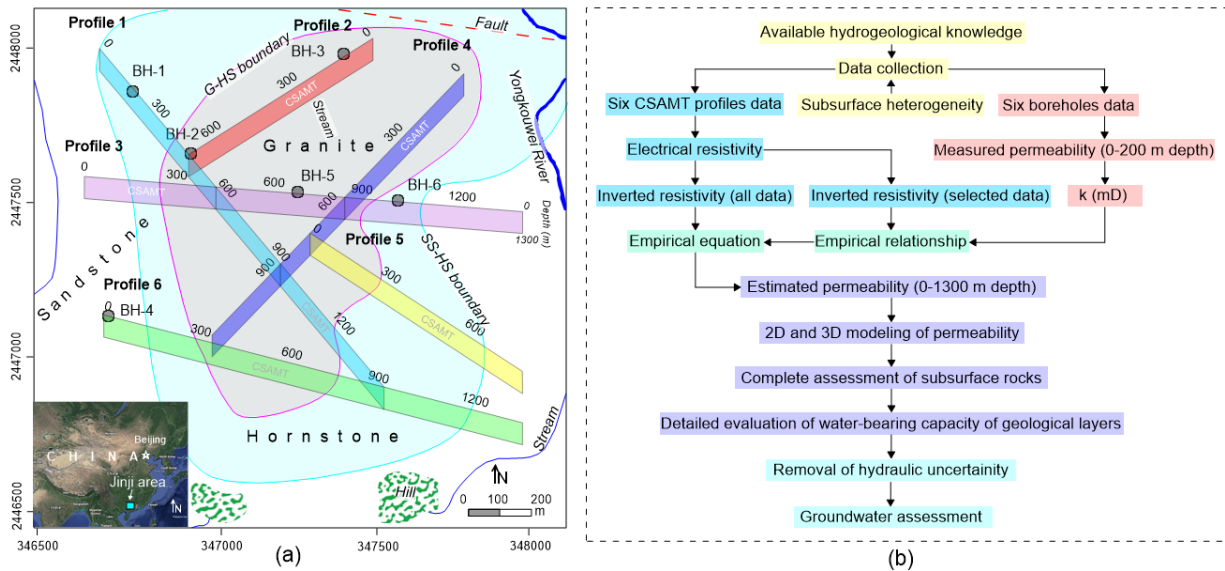
182 **Table 1**

Method	Typical depth of investigation	Spatial resolution	Cultural noise susceptibility	Cost and logistics	Suitability for deep hard rock aquifers
VES (Vertical Electrical Sounding)	<200 m	1D only, low lateral resolution	Low–Moderate	Low, rapid	Limited to shallow, homogeneous settings
ERT (Electrical Resistivity Tomography)	Up to ~300 m	High (2D/3D imaging)	Moderate	Moderate; requires dense electrode arrays	Excellent for shallow fractured/karst zones, but inadequate for >500 m depth
TDEM (Time-Domain Electromagnetics)	200–600 m (occasionally deeper)	Moderate	Moderate; affected by near-surface conductivity	Moderate, rapid deployment	Useful for intermediate depths; less effective in highly resistive hard rocks
MT (Magnetotellurics)	Hundreds of m to tens of km	Low in upper crust, improves at depth	High; strongly affected by cultural noise	High; long acquisition times	Excellent for regional mapping and geothermal studies; less suited for site-specific aquifer modeling
CSAMT (Controlled-Source Audio-MT)	~200–1,300 m (depending on frequency & geology)	Moderate–High (2D/3D capable)	Low; controlled source minimizes noise	Moderate; portable, adaptable	Well-suited for imaging deep, resistive, heterogeneous aquifers; strong balance of depth, resolution,

184

185 **2 Methods**

186 This research integrates limited drilling information with geophysical data to estimate k for both
 187 2D and 3D evaluations of groundwater resources over the entire investigated site (Fig. 1a). The
 188 main stages of the methodology are summarized in the flowchart shown in Fig. 1b.



189

190 **Fig. 1.** (a) The site map displaying six boreholes (BH-1 to BH-6) and six CSAMT survey profiles (1–6).
 191 The map also illustrates the simplified geological and hydrogeological setting, including the dominant
 192 rock types (granite, hornstone, and sandstone), the granite–hornstone (G–HS) and sandstone–hornstone
 193 (SS–HS) boundaries, major fault lines, streams, rivers, and surrounding mountainous terrain; (b)
 194 Flowchart illustrating the methodology for generating 2D and 3D k models to enable comprehensive
 195 assessments of groundwater resources across extensive areas

196 **2.1 Study area and hydrogeological settings**

197 This study is part of a national initiative in South Guangdong, China, focused on deep
198 subsurface exploration, including groundwater resource assessment and infrastructure
199 development such as the Jiangmen Underground Neutrino Observatory (JUNO) (Hasan et al.,
200 2025). These actions contribute to China's national agenda toward sustainable deep-earth
201 resource utilization. This research was conducted in the Jinji region, a geologically complex area
202 prioritized for deep groundwater exploration (Fig. 1a). The region lies within a subtropical
203 monsoonal climate zone, receiving ~1981 mm of annual rainfall. Topography ranges from low
204 hills to mountainous terrain (39–539.9 m elevation), with dense vegetation and varied slopes.
205 The northern part is relatively flat, while the south includes prominent features such as the
206 Dashishan and Qilongding Mountains. Surface drainage is primarily controlled by the
207 Yongkouwei River in the northeast.

208 Geologically, the Jinji area has evolved through successive tectono-magmatic processes
209 linked to the Yanshanian, Indosinian, and Caledonian mountain-building phases, resulting in a
210 lithologically diverse landscape of granite, sandstone, and hornstone (Qin, 2017). Granite
211 intrusions reflect deep crustal magmatism, while hornstone indicates contact metamorphism.
212 Overlying Paleogene sediments record later basin development. Tectonic structuring in the area
213 is largely influenced by the Kaiping fault-fold complex, which includes reverse, thrust, and
214 strike-slip faults formed under prolonged crustal compression and later modified by strike-slip
215 tectonics. These northeast-trending structures govern subsurface architecture and groundwater
216 flow pathways (Yang et al., 2021). Fractures and joints are widespread in granite, sandstone, and
217 hornstone, varying by lithology and tectonic history. These brittle features act as primary
218 conduits for groundwater, with their alignment along major faults highlighting the tight coupling
219 between structural geology and hydrogeology.

220 This study focuses on the vertical stratification of aquifer-bearing formations. Productive
221 groundwater is mainly stored in deep, fractured sandstone units, overlain by low-permeability
222 granite that limits vertical recharge. An intermediate hornstone layer separates the two, with
223 moderate hydraulic properties and limited connectivity. This configuration isolates the deep
224 aquifer from surface influences, rendering shallow investigations ineffective. Deep-targeted
225 exploration is thus essential for identifying and managing these concealed high-potential
226 groundwater resources in a structurally complex hard rock setting.

227 **2.2 CSAMT survey**

228 **2.2.1 Theoretical background**

229 CSAMT is extensively employed for hard rock evaluations due to its ability to resolve deep
230 subsurface features (Fu et al., 2013; Wang et al., 2015; Di et al., 2020; Kouadio et al., 2023).
231 This method employs a distant, regulated electric source that transmits signals into the ground,
232 while electric and magnetic field components are recorded at receiving stations (Zonge and
233 Hughes, 1991). CSAMT uses frequency-dependent EM wave penetration; lower frequencies
234 reach greater depths, depending on rock conductivity (Cagniard, 1953; Borah and Patro, 2019).
235 Signal frequencies are extracted using Fourier transforms from time-series field measurements
236 (Simpson and Bahr, 2005). A typical CSAMT setup uses electric dipole sources arranged
237 between 1 and 2 km intervals, with 5–10 km offsets based on the required penetration depth and
238 lithological conditions.

239 Resistivity is calculated by analyzing orthogonal electric and magnetic field magnitudes.
240 Vertical resolution typically ranges from 5%–20% of the depth of investigation (DOI), which
241 spans ~20–1000 m. Shallow depths (20–100 m) offer finer resolution, while deeper imaging is

242 coarser due to signal attenuation. DOI increases with lower frequencies and higher subsurface
243 resistivity (Borah and Patro, 2019). Lateral resolution depends on station spacing (10–200 m);
244 wider spacing enhances signal strength and coherence (Simpson and Bahr, 2005). Field setups
245 include portable receivers with electrodes and magnetic sensors to record signals, which are
246 filtered and amplified in real time. Effective survey planning is essential to mitigate interference
247 from fences, power lines, and radio transmitters. Final resistivity models are presented in plan,
248 fence, cross-sectional, or 3D formats.

249 **2.2.2 Survey design and procedures**

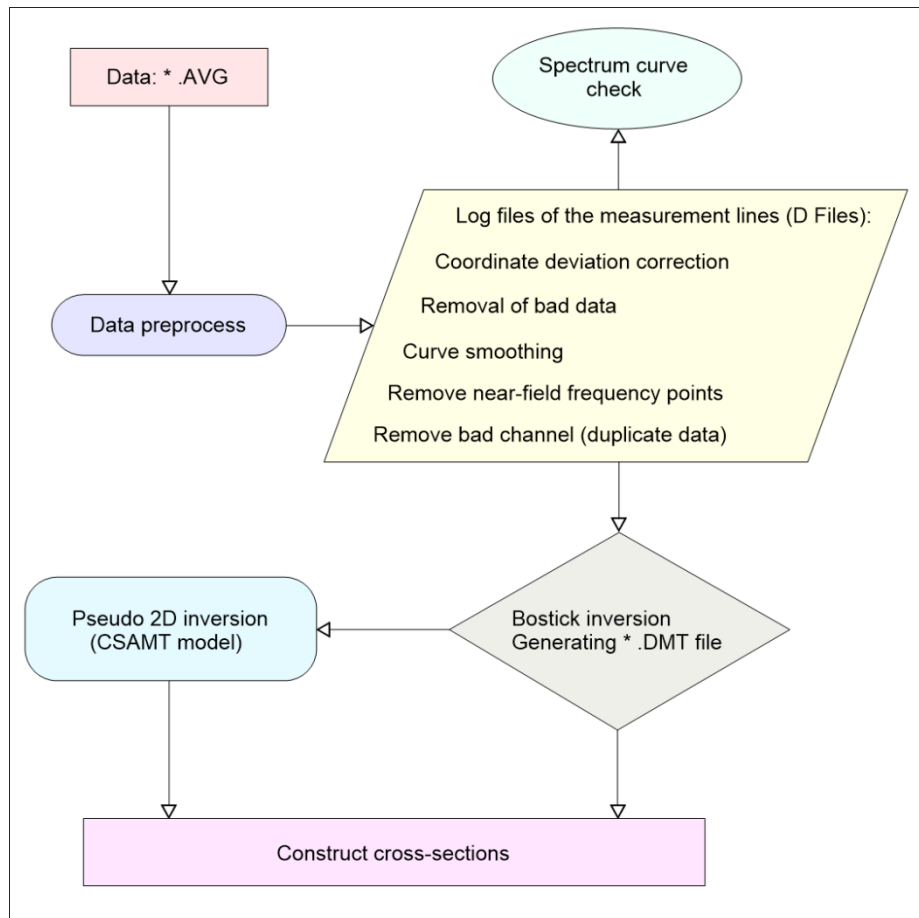
250 Data acquisition was performed along six CSAMT lines (1–6) using a 50 m interval between
251 stations, selected based on geological targets, terrain accessibility, structural orientation,
252 integration with borehole data, and expected resistivity contrasts. These optimized profiles
253 improved subsurface resolution and minimized interpretational ambiguity. The DOI reached
254 approximately 1300 m. Measurements were conducted in scalar Transverse Magnetic (TM)
255 mode, recording E- and H-field vectors in both longitudinal and transverse directions along the
256 survey profiles. EMAP stations were spaced ~50 m from electrodes. A 50 Hz linear filter was
257 implemented under Gain Mode X1 settings. Transmission current spanned 2.6–18 A across the
258 7680 Hz to 1 Hz range.

259 Data acquisition utilized a Phoenix Geophysics V8 multifunction receiver and TXU-30
260 transmitter, capable of 30 kW output, transmitting up to 1000 V and 40 A. The system operated
261 across 34 frequencies (1–7680 Hz), with transmitter–receiver distances of 9.3–12.5 km. Non-
262 polarized electrodes captured electric fields, while magnetic fields were recorded using AMTC-
263 30 sensors (0.1–10,000 Hz). Each site recorded two orthogonal electric and three orthogonal
264 magnetic components, enabling full impedance tensor calculation. Survey positions were

265 determined using Hi-Target V30 RTK and Trimble XH GPS, ensuring sub-meter accuracy.
266 Coordinates were computed and transmitted to the navigation system for real-time positioning.
267 Survey point spacing remained consistent, with system quality metrics indicating 3–5%
268 variability. Design tolerances were met: RMS error $< \pm 5\%$, inter-point error $< 10\%$, horizontal
269 and vertical tolerances of 2.33 mm and 1.67 mm, respectively. Minimal anthropogenic and
270 electrical interference at the site resulted in high-quality data. Final site interpretation was based
271 on rigorous CSAMT data processing, including skew filtering and curve analysis (Hasan et al.,
272 2025).

273 **2.2.3 Processing workflow**

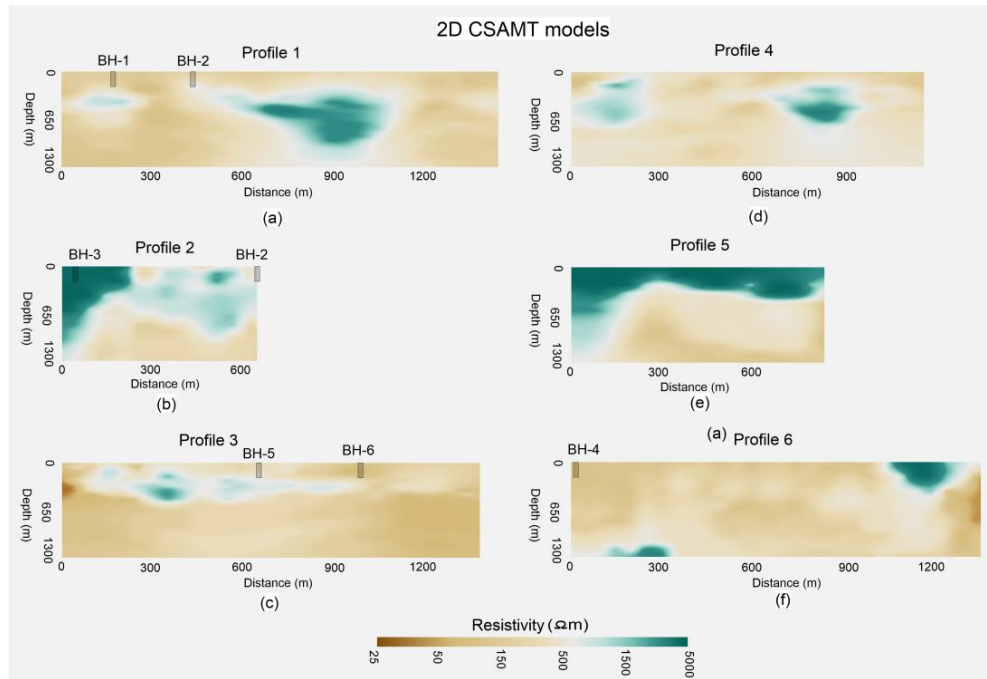
274 Spatial filters (Hanning window) and static corrections were applied to refine resistivity data and
275 enhance the model accuracy. The static corrections addressed near-surface resistivity
276 inhomogeneities that cause vertical shifts in apparent resistivity curves. By calibrating electric
277 field measurements to a stable reference, shallow-layer effects were minimized, isolating deeper
278 signals. Spatial filtering using a Hanning window reduced high-frequency noise while preserving
279 coherent spatial patterns. This approach significantly improved inversion model stability by
280 suppressing spectral leakage and smoothing fluctuations. Data processing was carried out using
281 the CMTPro version software produced by Phoenix Geophysics (Phoenix Geophysics CMTPro,
282 2020), which integrates V8 and tracking data, corrects coordinates, smoothes curves, and exports
283 files for inversion. Based on CSAMT-SW technique, the processing workflow shown in Fig. 2
284 (Phoenix Geophysics CSAMT-SW, 2020) was conducted to obtain 2D inversion (Rodi and
285 Mackie, 2001; Wang et al., 2015).



286

287 **Fig. 2.** Schematic of the 2D CSAMT data inversion workflow using Bostick methodology

288 The main components of the CSAMT-SW framework are: 1. Transformation from AVG
 289 to D format; 2. Editing CHK data and converting to D format; 3. Manual data checks: gap filling,
 290 near-field removal; 4. Smoothing based on D-format data; 5. Estimation of correction factors (D,
 291 H, K, Z); 6. The Bostick inversions; 7. The Quasi-2D inversions using the global field model
 292 (ID), integrating near and transition fields. Post-Bostick inversion results were stored as
 293 *_BOS.DAT and *_BSS.DAT, with final inversion-ready data in *_M.DMT. The 2D inversion
 294 proceeded until either the RMS error threshold or a five-iteration limit was reached. Final
 295 resistivity models (Fig. 3) were cross-validated with local geology and clearly delineated
 296 subsurface features, offering a robust interpretation framework.



297

298 **Fig. 3.** Construction of 2D CSAMT models along six geophysical surveyed lines: (a) Line 1, (b) Line 2,
 299 (c) Line 3, (d) Line 4, (e) Line 5, and (f) Line 6. Resistivity values increase from brown to green on the
 300 color scale.

301 2.3 Permeability estimation framework

302 2.3.1 Laboratory-based permeability determination from borehole core samples

303 Permeability is a key hydrogeological parameter that quantifies the ability of porous media, such
 304 as rock or sediment, to transmit fluids. It governs subsurface fluid flow and plays a central role in
 305 groundwater studies (Allègre et al., 2016; Fiandaca et al., 2018; Mudunuru et al., 2022;
 306 Esmailpour et al., 2023; Carbillet et al., 2024). Permeability reflects how easily fluids move
 307 through pore networks or fractures and is typically measured via pumping tests or core analysis,
 308 methods that are costly and logistically intensive. It is influenced by porosity, lithology,
 309 saturation, structural features (e.g., faults, joints), and diagenetic processes (Dewandel et al.,
 310 2006; Yan et al., 2024).

311 In this study, initial k data from the Jinji region were limited to six boreholes. To
312 strengthen the dataset, 116 lab tests were conducted on core samples from three main lithologies,
313 sandstone (31), hornstone (23), and granite (62), recovered from depths up to 200 m. These data
314 help delineate vertical k trends and refine the region's hydrogeological model. Core recovery
315 employed a wireline rotary system with triple-tube barrels to preserve sample integrity (ISRM,
316 2015). Samples were vacuum-sealed and stored under controlled humidity to retain in-situ
317 moisture and fracture structure. Prior to testing, cores were trimmed to standard 50 mm ×
318 100 mm cylinders and screened for visible defects. Two laboratory methods were used based on
319 k range. The steady-state flow test with ASTM D5084-21 guidelines (ASTM, 2021) was applied
320 to higher- k sandstone. A constant hydraulic gradient was applied under fully saturated
321 conditions, and the corresponding volumetric flow rate was recorded. Permeability was
322 determined through the application of Darcy's Law:

$$323 \quad k = \frac{Q \cdot \mu \cdot L}{A \cdot \Delta P} \quad (1)$$

324 where ΔP is the pressure differential applied across the sample (Pa), A is the cross-sectional area
325 (m^2), L is the length of the sample (m), μ is the dynamic viscosity of the fluid (Pa·s), and Q is the
326 volumetric flow rate (m^3/s).

327 For low- k hornstone and granite, the pulse decay method (Brace et al., 1968) was used. A
328 brief pressure pulse was applied, and pressure decay was monitored under confining stresses up
329 to 30 MPa to simulate in-situ conditions and assess stress-dependent k behavior. Tests were
330 conducted under both dry and saturated conditions to evaluate moisture sensitivity. Replicate
331 measurements ensured data reliability, and statistical analyses assessed intra- and inter-lithology
332 variability. Results revealed that granite had the lowest k due to its dense crystalline structure,

333 while hornstone showed intermediate values, likely due to localized fracturing. Sandstone
334 exhibited the highest k , particularly at greater depths, confirming its role as the primary aquifer
335 unit in the region.

336 **2.3.2 Permeability-resistivity relationship: Archie’s law and the role of Kozeny–Carman**

337 Numerous foundational studies have linked electrical resistivity to hydraulic properties like k . A
338 prominent example is the Archie equation (Archie, 1942), which relates resistivity to porosity
339 and water saturation in clean, saturated sediments. However, its assumption of clay-free
340 conditions limits its applicability in complex or clay-rich lithologies (Waxman and Smits, 1968;
341 Glover, 2015). It is commonly expressed as:

$$342 \quad \rho b = a \cdot \rho f \cdot \phi^{-m} \quad (2)$$

343 In this equation, ϕ is porosity, ρf is fluid resistivity, ρb is bulk resistivity, and a and m are
344 empirical constants. Although Archie’s law does not directly yield k , porosity serves as a useful
345 proxy due to its strong influence on fluid movement. As such, the resistivity–porosity
346 relationship can be leveraged to infer k indirectly, especially when supplemented with additional
347 petrophysical frameworks (Revil and Cathles, 1999).

348 The Kozeny–Carman equation, though not used explicitly in this study, provides a widely
349 accepted theoretical foundation that connects k to porosity and specific surface area (DallaValle,
350 1956; Bear, 1972). While it does not incorporate resistivity directly, this model is often used in
351 hydrogeophysical studies to support the interpretation of petrophysical relationships that bridge
352 electrical and hydraulic properties (Chapuis and Aubertin, 2003). Its relevance lies in the broader
353 theoretical justification for using porosity, derived or inferred from resistivity, as a predictor of k .

354 The application of this equation alongside Archie’s law facilitates the development of empirical
355 or semi-empirical models that connect electrical resistivity to k (Glover, 2009; Yan et al., 2024).

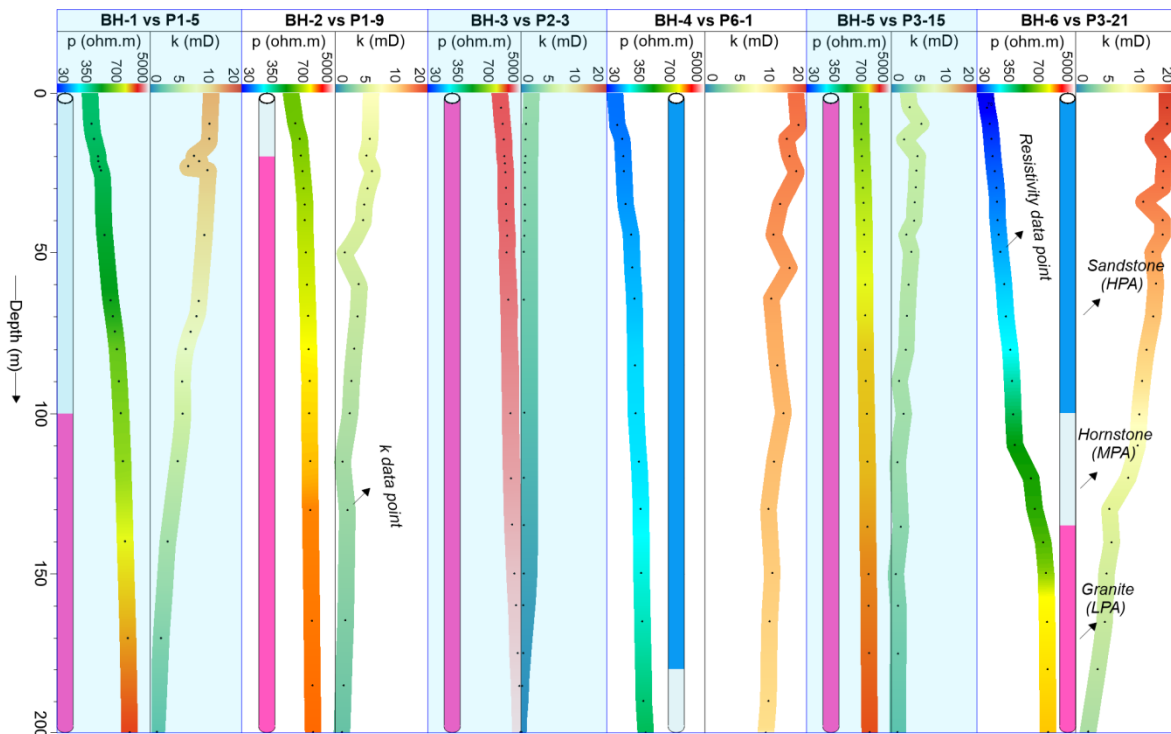
356 However, direct application of these equations to complex geological environments, such
357 as fractured granite, sandstone, and hornstone, remains limited due to heterogeneities in mineral
358 composition, pore connectivity, and structural anisotropy. To mitigate such constraints, our
359 approach empirically develops a localized, site-calibrated correlation involving k and resistivity,
360 grounded in co-located deep borehole and CSAMT data. This empirical link supports high-
361 resolution spatial modeling of k in both 2D and 3D for the Jinji area, offering enhanced insight
362 into subsurface hydrogeological conditions where traditional models may not be applicable.

363 **2.3.3 Spatial permeability modeling from CSAMT data**

364 To estimate permeability across the entire study area, we employed a multi-stage approach
365 integrating borehole core analysis with CSAMT-derived resistivity data. In the first stage, a total
366 of 116 laboratory-based k measurements were acquired using 6 drilling tests (from BH-1 to BH-6)
367 with 0–200 m depth (Fig. 4). The k measurements were obtained from intact rock core samples
368 representing three principal lithologies: granite, hornstone, and sandstone.

369 In the second stage, each of the 116 borehole-derived k values was empirically correlated
370 with corresponding resistivity values extracted from CSAMT soundings co-located with the
371 borehole sites. The spatial correspondence between boreholes and CSAMT sounding points was
372 carefully matched (Fig. 4). For example: P1-5 represents the fifth CSAMT sounding at 200 m
373 along survey line 1 near borehole BH-1; P1-9 corresponds to the ninth sounding at 400 m on line
374 1 near borehole BH-2; P2-3 denotes the third sounding at 100 m along line 2 near BH-3; P6-1
375 indicates the first sounding at 0 m on line 6 adjacent to BH-4; P3-15 and P3-21 represent the

376 fifteenth (700 m) and twenty-first (1000 m) soundings along line 3, near boreholes BH-5 and
 377 BH-6, respectively.



378

379 **Fig. 4.** Comparison of 116 CSAMT-based resistivity (ρ) data points with corresponding drilling-based
 380 permeability (k) values at depths of 0–200 m across six borehole locations (BH-1 to BH-6). The data were
 381 used to evaluate high potential aquifers (HPA) in sandstone, medium potential aquifers (MPA) in
 382 hornstone, and low potential aquifers (LPA) in granite. Each dot represents a resistivity or permeability
 383 data point. Sounding labels indicate specific CSAMT locations: P1-5 (5th point on line 1), P1-9 (9th on
 384 line 1), P2-3 (3rd on line 2), P6-1 (1st on line 6), and P3-15 and P3-21 (15th and 21st on line 3)

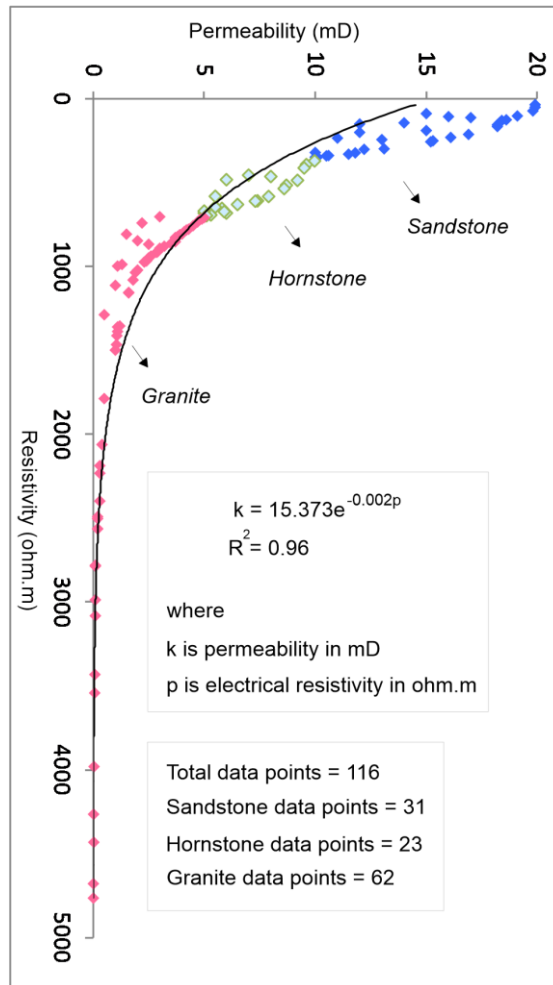
385 In the third stage, all 116 paired measurements of k and ρ were utilized to develop an
 386 empirical model. An exponential relationship was derived between permeability (k in
 387 millidarcies or mD) and electrical resistivity (ρ in Ω m), expressed as follows (Fig. 5):

388

$$k = 15.373 e^{-0.002\rho} \quad (3)$$

389 This site-specific empirical model was then applied to the entire suite of CSAMT resistivity data
390 collected along six survey profiles to estimate spatial variations in k across the broader study area.
391 Using this relationship, we generated predictive 2D and 3D k models that capture the hydraulic
392 behavior of three major lithological units: low potential aquifer (LPA): associated with low-
393 permeability granite, medium potential aquifer (MPA): hosted within fractured hornstone
394 (hornfels), high potential aquifer (HPA): corresponding to more porous sandstone units.

395 These models provide a depth-resolved assessment of subsurface k reaching depths of up
396 to 1300 m below the surface. Final 2D and 3D spatial visualizations were developed by SKUA-
397 GOCAD and Geosoft Oasis montaj modeling software (Webring, 1981; Mira Geoscience Ltd.,
398 1999; Hasan et al., 2024), enabling the visualization of k distributions across all six CSAMT
399 profiles and improving hydrogeological characterization in structurally complex hard rock terrain.



400

401 **Fig. 5.** Empirical relationship derived from 116 data points comparing CSAMT-based resistivity and
402 drilling-based k at depths of 0–200 m, across three lithologies: sandstone (31 data points), hornstone (23
403 data points), and granite (62 data points).

404 **3 Results**

405 **3.1 Cross-validation of geophysical and borehole parameters**

406 Table 2 summarizes the integrated dataset from 6 drills and 6 geophysical profiles to resolve the
407 spatial structure of the subsurface into three distinctive hydrogeological units, based on
408 variations in electrical resistivity and corresponding k values. The development of these

409 subsurface models mainly depends on borehole data, CSAMT-derived resistivity measurements,
 410 and the regional geological framework. The stratigraphy was categorized into three primary
 411 lithologies: sandstone, hornstone, and granite. Classification criteria were established as follows:
 412 sandstone was defined by resistivity values below 350 Ωm and a k range of 10–20 mD;
 413 hornstone exhibited resistivity values between 350 and 700 Ωm with a k range of 5–10 mD; and
 414 granite was characterized by resistivity values exceeding 700 Ωm and k values ranging from 0 to
 415 5 mD. Based on our evaluations of the subsurface hydrogeological model's aquifer potential
 416 zones, we found that sandstone contains the high potential aquifer (HPA), hornstone contains
 417 medium potential aquifer (MPA), and granite has low potential aquifer (LPA). Aquifers with the
 418 largest yields or the best water-bearing capacity are indicated by sandstone, whereas aquifers
 419 with the lowest yields or the worst water-bearing capacities are denoted by granite. Groundwater
 420 development is best facilitated by sandstone in the study area, whereas groundwater extraction is
 421 most hindered by granite.

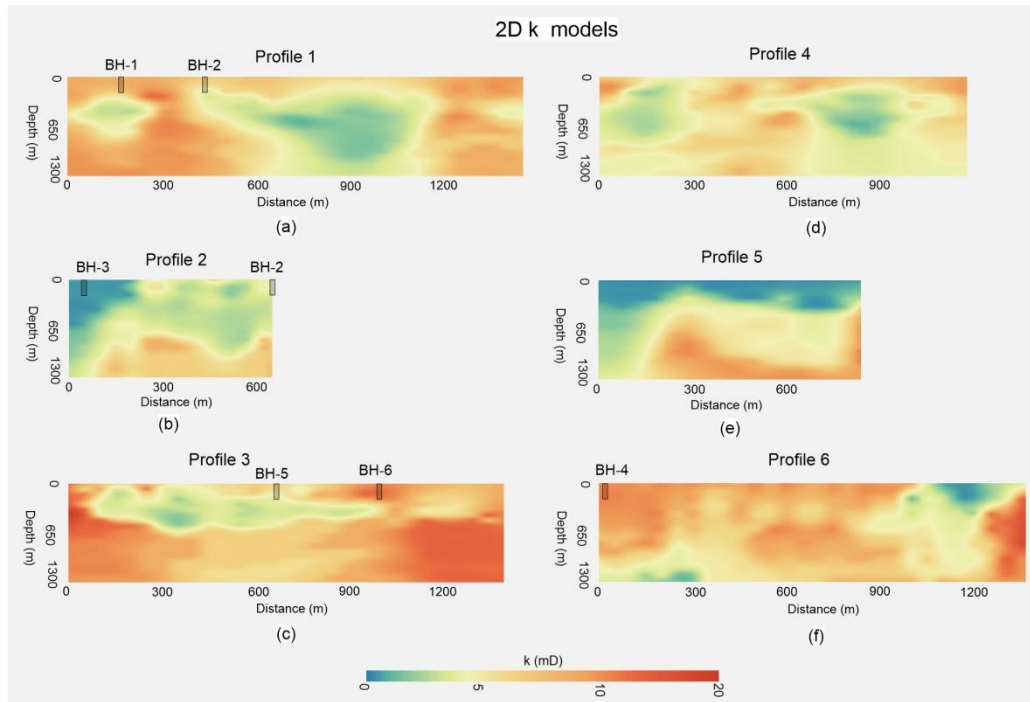
422 **Table 2**

423 Integrating distinct ranges of electrical resistivity and k enables a comprehensive assessment of
 424 groundwater potential across various hard rock types

Resistivity (Ωm)	k (mD)	Type of rock	Aquifer potential
< 350	10–20	Sandstone	High potential aquifer (HPA)
350–700	5–10	Hornstone	Medium potential aquifer (MPA)
>700	0–5	Granite	Low potential aquifer (LPA)

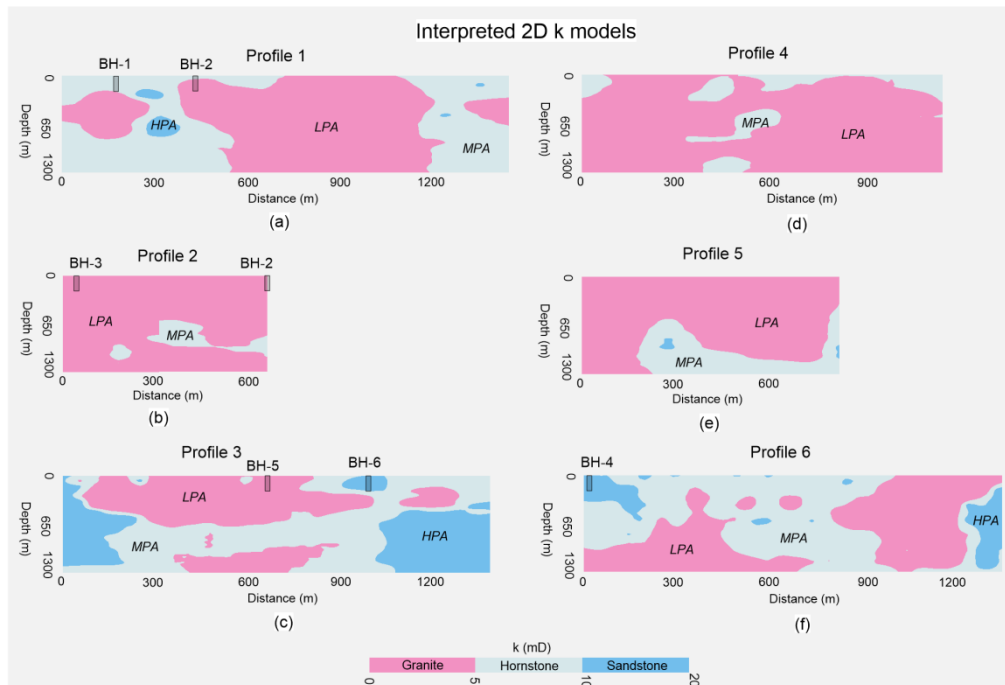
425 **3.2 2D groundwater assessments**

426 Using geophysical-borehole correlation as its basis, Eq. (3) efficiently converts 2D CSAMT
427 models (Fig. 3) into 2D k models (Fig. 6). The interpreted 2D k models shown in Fig. 7, in
428 comparison with the limited borehole experiments, allow for a comprehensive assessment of the
429 groundwater resources in hard rock across the whole research area, from 0 to 1300 m deep.



430

431 **Fig. 6.** The predicted 2D k models along six geophysical surveyed lines: (a) Line 1, (b) Line 2, (c) Line 3,
432 (d) Line 4, (e) Line 5, and (f) Line 6. k values increase from blue to red on the color scale.

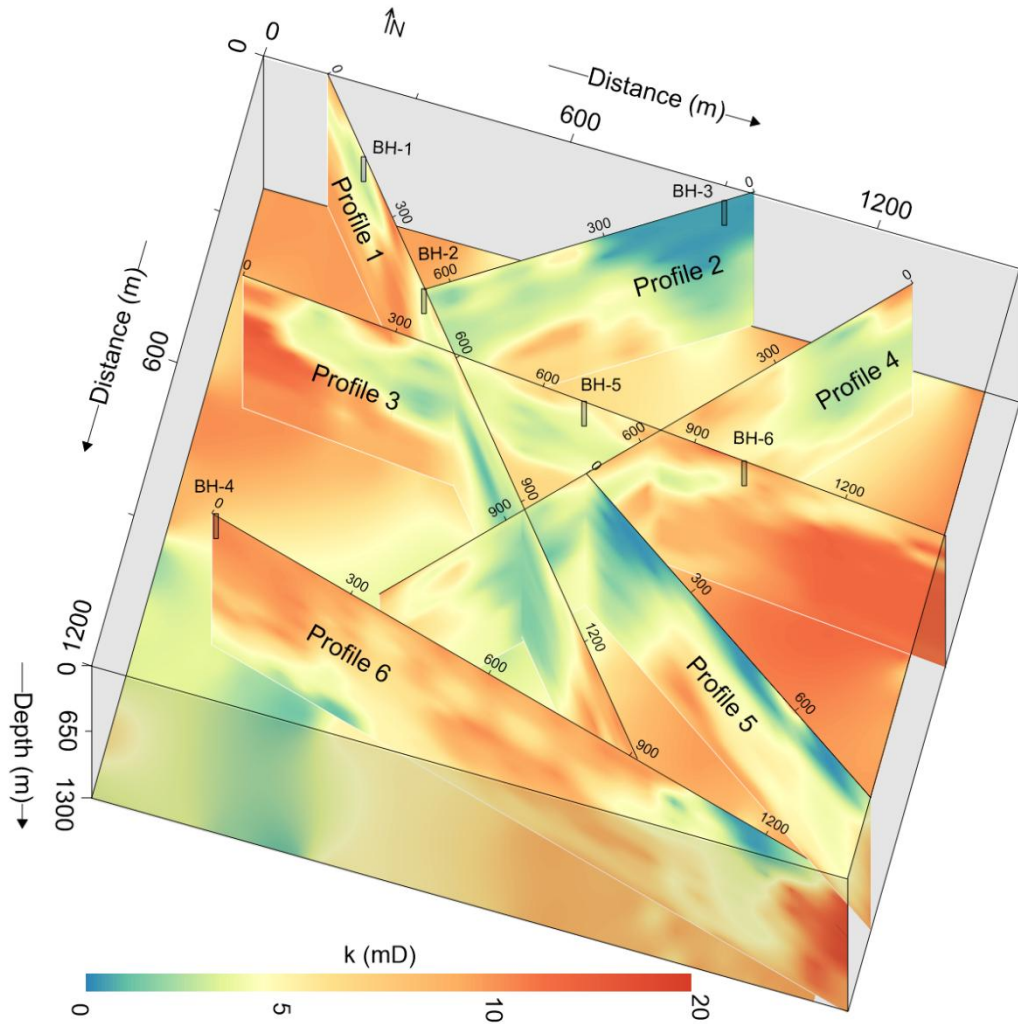


433

434 **Fig. 7.** The interpretation of the predicted 2D k models along six geophysical surveyed lines: (a) Line 1,
 435 (b) Line 2, (c) Line 3, (d) Line 4, (e) Line 5, and (f) Line 6. Sandstone is represented in blue, hornstone in
 436 light blue, and granite in pink

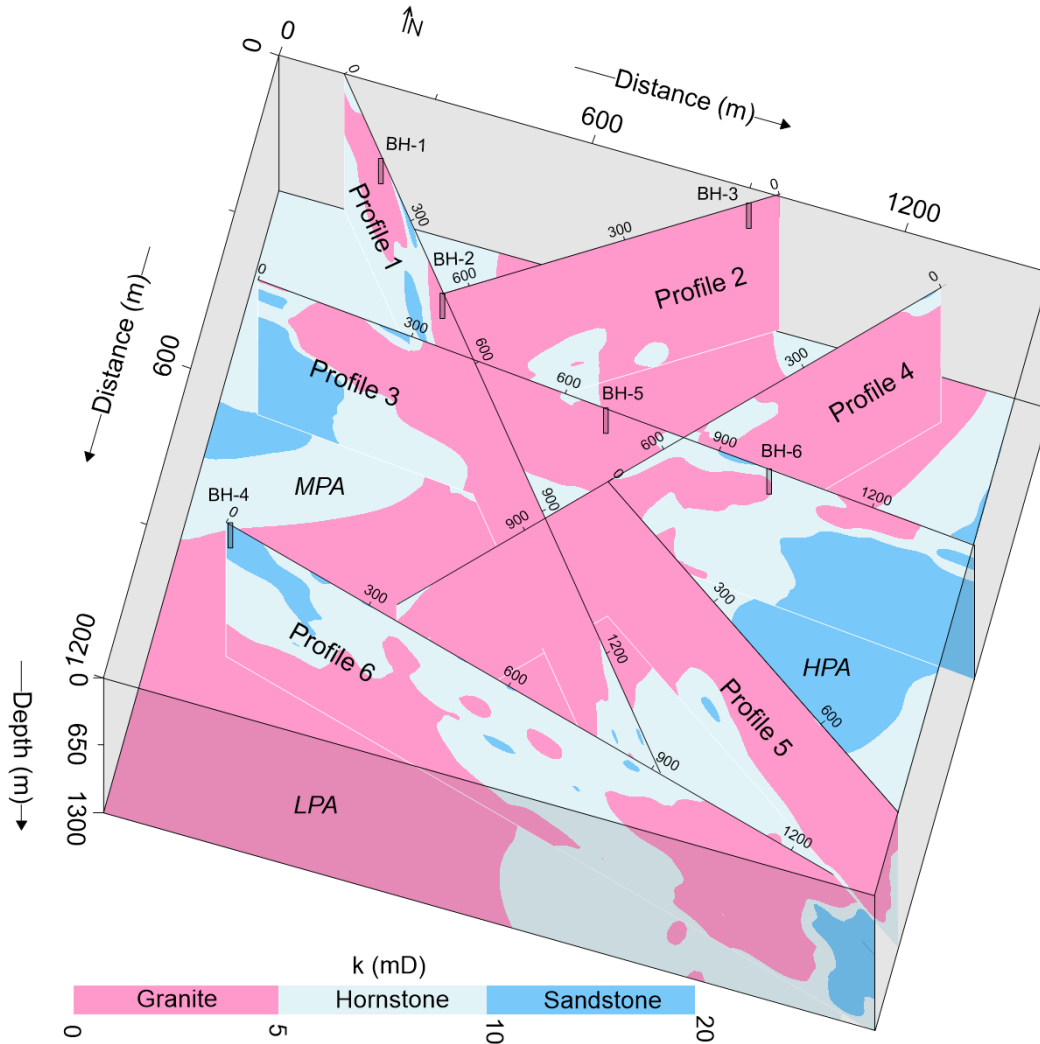
437 The integrated 2D k models (Fig. 8) and their interpretations (Fig. 9) provide a detailed
 438 evaluation of groundwater potential across complex geological settings of sandstone, hornstone,
 439 and granite. Profile 1 reveals a high-potential sandstone aquifer (85–305 m thick) between 245–
 440 380 m distances at 205–400 m depth. Medium-potential hornstone aquifers are found from 0–
 441 525 m and 1185–1445 m distance down to 1300 m. Low-potential granite aquifers appear at 0–
 442 285 m (290–790 m depth), 385–1185 m (full depth), and 1305–1450 m (390–745 m depth).
 443 Profile 2 shows a medium-potential hornstone aquifer with 140–380 m thickness (490–1105 m
 444 depth) between 145–215 m and 290–645 m distance. No high-potential sandstone aquifers are
 445 present. Granite dominates (0–700 m distance, 0–1300 m depth) the profile with low yield except
 446 in hornstone zones. Profile 3 contains both high-potential sandstone (0–250 m, 905–1065 m, and

447 1040–1390 m distances at respective depths of 0–1190, 0–205, and 490–1305 m) and medium-
448 potential hornstone aquifers (full depth with 0–1400 m distance) across the entire surveyed line.
449 Granite aquifers are assessed at 80–1015 m (0–590 m depth), 395–845 m (915–1300 m depth),
450 and 1100–1300 m (200–500 m depth). Profile 4 features medium-potential hornstone at 0–105 m
451 (0–340 m depth), 340–645 m (0 to 1300 m depth), 595–790 m (0–300 m depth), and 1015–1145
452 m (0–345 m depth). No high-potential sandstone is observed. Granite aquifers of low potential
453 dominate (0–1145 m distance between 0–1300 m depth), except in hornstone zones. Profile 5
454 shows medium-potential hornstone (190–845 m distance, 390–1300 m depth) and two small
455 high-yield sandstone patches (290 m at 790–960 m depth and 815 m at 1045–1135 m depth).
456 Low-potential granite appears at distance 0–190 m (0–1300 m depth) and 790–815 m (0–1025 m
457 depth). Profile 6 includes high-potential sandstone zones at 0–190 m (0–490 m depth) and 1245–
458 1345 m (215–1225 m depth). Low-potential granite is present at 0–690 m (390–1300 m depth)
459 and 790–1360 m (0–1190 m depth), while hornstone with medium potential dominates the
460 remainder. Overall, the southeastern and northwestern zones host abundant medium- to high-
461 potential aquifers, while central regions show limited or poor groundwater prospects.



462

463 **Fig. 8.** The integrated 2D k models derived from the incorporation of geophysical and drilling data, with k
 464 represented on a color bar spanning from green to red



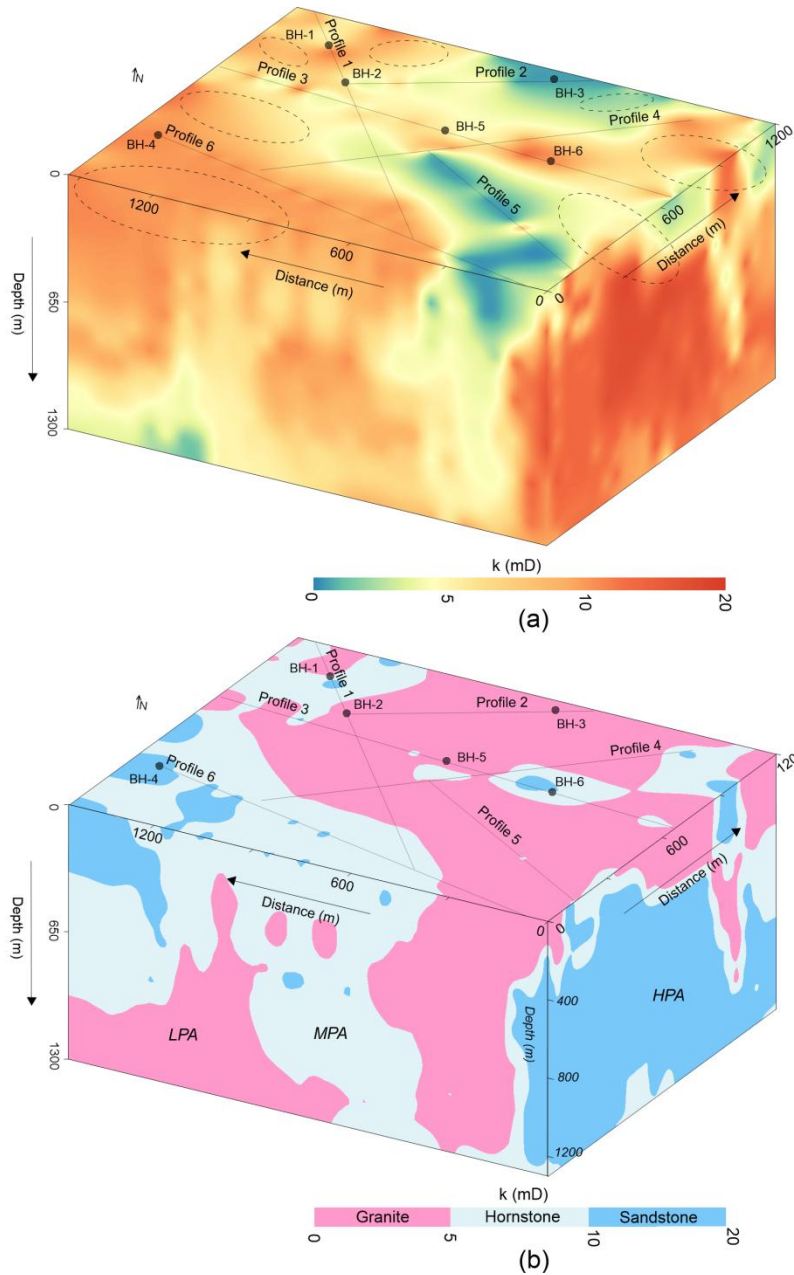
465

466 **Fig. 9** Analysis of 2D k models, based on defined k ranges, for three groundwater potential aquifers: low
 467 potential aquifer (LPA), medium potential aquifer (MPA), and high potential aquifer (HPA),
 468 corresponding to the granite, hornstone, and sandstone formations, respectively

469 **3.3 3D groundwater assessments**

470 The 3D k (outer view) visualization (Fig. 10a, b) provides a comprehensive assessment of the
 471 water-bearing capacity of the rock mass. Low-potential granite aquifers are found at the surface
 472 along: line 1 (85–215 m, 385–1175 m), line 2 (0–655 m), line 3 (0–45 m, 95–175 m, 265–585 m,
 473 605–845 m, 1145–1315 m), line 4 (90–390 m, 490–615 m, 745–1115 m), line 5 (0–815 m), and

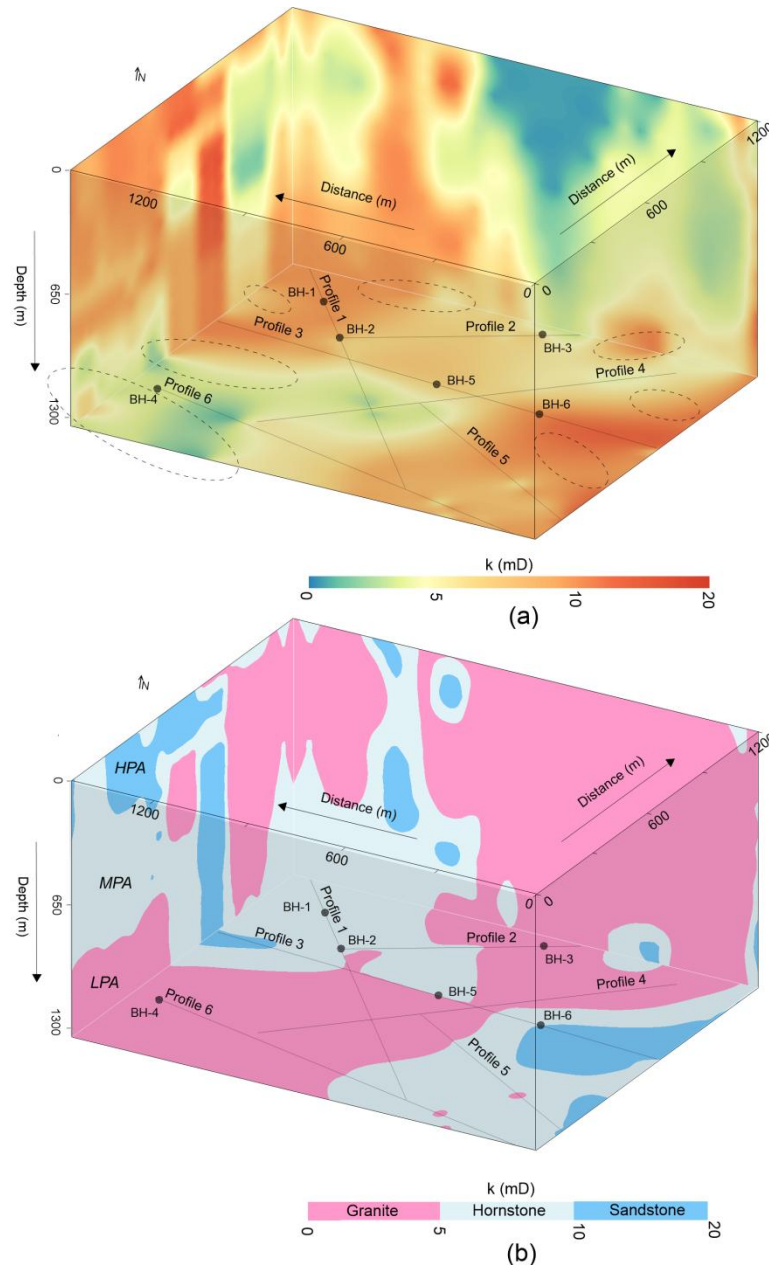
474 line 6 (1045–1345 m). Medium-potential hornstone aquifers appear along: line 1 (0–95 m, 190–
475 260 m, 295–415 m, 1185–1425 m), line 3 (40–105 m, 215–275 m, 580–605 m, 850–910 m,
476 1010–1155 m, 1310–1410 m), line 4 (45–90 m, 390–490 m, 590–685 m, 1115–1185 m), and line
477 6 (90–190 m, 215–275 m, 315–485 m, 505–605 m, 635–1045 m). High-potential sandstone
478 aquifers are identified in: line 1 (265–310 m), line 3 (235–255 m, 915–1010 m), line 4 (0–45 m),
479 and line 6 (0–90 m, 210–225 m, 275–305 m, 515–525 m, 605–635 m), Overall, Fig. 10 (a, b)
480 shows that higher-yield aquifers are mainly concentrated in the southern portion of the
481 investigated site.



482

483 **Fig. 10.** The 3D k models (CSAMT-based), with k shown on a color scale increasing from green to red,
 484 correspond to three groundwater potential aquifers: low potential aquifer (LPA), medium potential aquifer
 485 (MPA), and high potential aquifer (HPA), associated with three geological strata: granite, hornstone, and
 486 sandstone, respectively. The uncertainty contours (highlighted by areas with black dots) indicate zones of
 487 reduced confidence in k estimation. (a) The exterior visualization of the 3D k model, and (b) The analysis
 488 of the 3D k model from an external perspective

489 Fig. 11 (a, b) shows a 3D internal view of aquifer potential at 1300 m depth. Low-yield
490 granite aquifers are identified along: surveyed line 1 (515–1215 m), line 2 (0–290 m), line 3
491 (390–690 m), line 4 (0–1145 m), line 5 (0–195 m, 565–595 m), and line 6 (0–690 m, 1075–1115
492 m). Medium-potential hornstone aquifers are found along: profile 1 (0–540 m, 1215–1445 m),
493 profile 2 (295–675 m), profile 3 (175–395 m, 445–815 m, 915–1035 m), profile 5 (205–565 m,
494 610–815 m), profile 6 (685–1080 m, 1110–1355 m). High-potential sandstone aquifers appear
495 along: profile 3 (0–205 m, 1010–1400 m) and profile 5 (810–815 m). Overall, medium to high
496 potential aquifers are mainly distributed in the southeastern and northwestern regions, while
497 central areas are dominated by low-yield granite. The aerial 3D k model enhances visualization
498 of aquifer distribution, supporting accurate groundwater assessment.



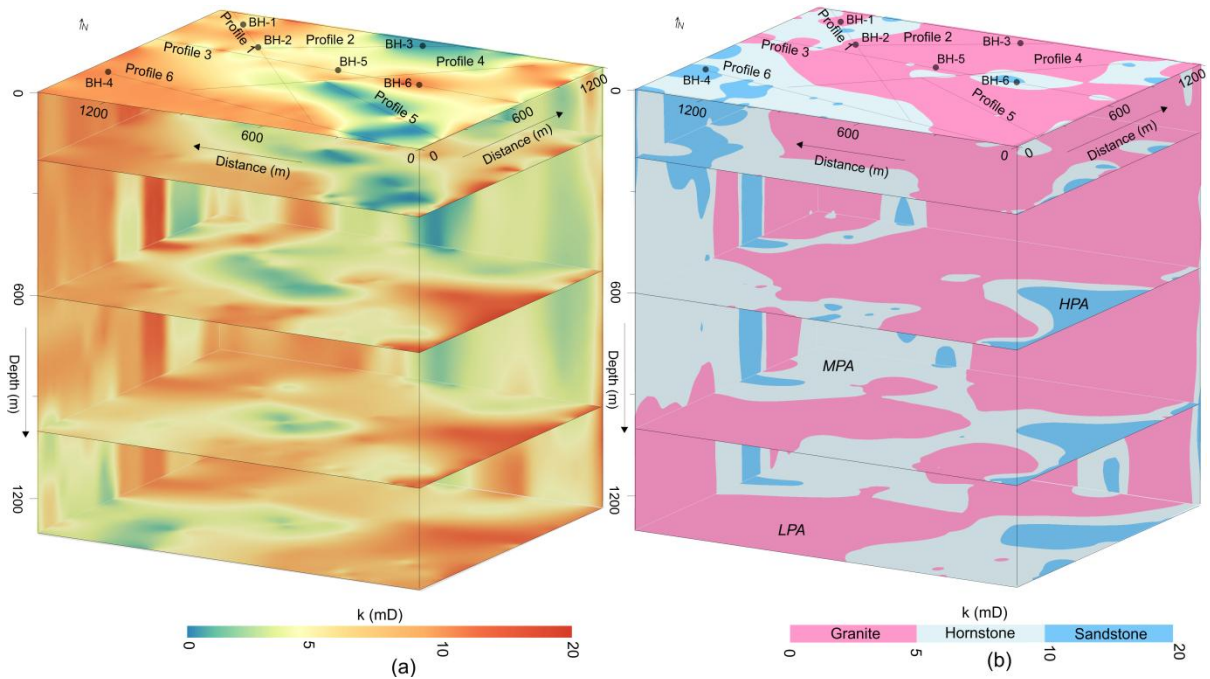
499

500 **Fig. 11.** The 3D k models (CSAMT-based), with k represented on a color scale ranging from green to red,
 501 illustrate three groundwater potential aquifers: low potential aquifer (LPA), medium potential aquifer
 502 (MPA), and high potential aquifer (HPA), associated with three geological strata: granite, hornstone, and
 503 sandstone, respectively. The uncertainty contours (highlighted by areas with black dots) indicate zones of
 504 reduced confidence in k estimation. (a) The interior visualization of the 3D k model, and (b) The analysis
 505 of the 3D (internal perspective) k model

506 3.4 Depth-wise groundwater assessments

507 Due to limited borehole data, direct estimation of k below 200 m is not feasible.
508 However, by integrating borehole and CSAMT data, k values could be reliably estimated down
509 to 1300 m. This approach enabled efficient and detailed evaluation of hard rock aquifers using
510 both 2D and 3D models (Fig. 12), with k values extracted at depths of 0, 200, 600, 1000, and
511 1300 m. At 1300 m, over 42% of the subsurface in the southwest and northeast comprised low-
512 yield granite. Hornstone accounted for 40% (medium yield) near granite zones in the northwest
513 and southeast, while high-yield sandstone made up 18% in the east. At 1000 m, sandstone (15%)
514 was concentrated in the southeast (high yield), hornstone (38%) in the southeast and northwest
515 (medium yield), and granite (47%) dominated the central and boundary zones (low yield). At
516 600 m, the subsurface was 55% granite (central and northern zones, low yield), 32% hornstone
517 (western region, medium yield), and 13% sandstone (southeast, high yield). At 200 m, granite
518 dominated 64% of the center and north (low yield), hornstone made up 26% in the south
519 (medium yield), and sandstone (10%) in the west was associated with high yield. At 0 m, 73% of
520 the central area comprised low-yield granite, 20% of the southwest was hornstone (medium
521 yield), and 7% sandstone (high yield) was concentrated in the southwest.

522 Overall, Fig. 12 shows a decrease in low-yield granite thickness with depth. Groundwater
523 potential is lowest around 600–700 m depth, while deeper zones (>700 m) in the northwest,
524 southeast, and southwest show more favorable aquifer conditions.



525

526 **Fig. 12.** (a) Geophysical k imaging at depths of 0, 200, 600, 1000, and 1300 m, with k shown on a color
 527 scale increasing from green to red. (b) Evaluation of CSAMT-derived k values (based on defined k ranges)
 528 at various depths for different aquifer types: low potential aquifer (LPA) in granite, medium potential
 529 aquifer (MPA) in hornstone, and high potential aquifer (HPA) in sandstone

530 **3.5 Validation of predicted vs. measured permeability**

531 Groundwater evaluation was greatly improved by systematic CSAMT-based k estimation. As
 532 shown in Figs. 6–12, granite dominates the central, northeastern, and southwestern zones;
 533 hornstone occurs mainly in the southeast, west, and northwest; and sandstone is prevalent in the
 534 east. Borehole-based assessments are limited by inconsistent subsurface mapping. While k values
 535 align near 200 m depth, broader extrapolation remains uncertain, highlighting the limitations of
 536 sparse drilling in complex geology.

537 To clarify the basis of the percentage matching values, the following explicit equation
538 was used to quantify the agreement between CSAMT-derived k' values and borehole-based k
539 estimates:

$$540 \quad \text{Percentage Match} = \left(\frac{\min(k, k')}{\max(k, k')} \right) \times 100 \quad (4)$$

541 Here, $\min(k, k')$ is the smaller of the two permeability values, either the measured permeability
542 (k) from borehole data or the estimated permeability (k') from the CSAMT model, at a given
543 depth. Conversely, $\max(k, k')$ is the larger of the two values. This ratio offers a normalized
544 agreement metric, where 100% indicates a perfect match and lower values reflect greater
545 divergence. Comparisons were made at multiple depth intervals across six calibration boreholes.
546 Table 3 summarizes the percentage agreement for 18 selected data points (out of 116) between
547 measured and predicted k values. Agreement was calculated at matched depth intervals for each
548 borehole–sounding pair using Eq. (3). For example, BH-1 and P1-5 show 73%, 63%, and 100%
549 agreement at 10, 40, and 170 m depth. BH-2 and P1-9 exhibit 80%, 77%, and 85% agreement at
550 20, 60, and 185 m depth. Other pairings, such as BH-3 with P2-3, show lower agreement (67%,
551 40%, 30%) at 10, 85 and 200 m depth, while BH-5 and P3-15 yield high matches of 80%, 94%,
552 and 85% at 30, 135, and 200 m depth, and BH-6 and P3-21 produce matches of 61%, 74%, and
553 71% at 45, 165, and 180 m depths, respectively.

554 Overall, the results indicate strong consistency between observed and predicted k values,
555 with discrepancies likely due to local heterogeneity or measurement uncertainty. Even at lower
556 percent match, both methods often classify the site into the same aquifer potential zone,
557 supporting the robustness of the CSAMT-based approach for regional groundwater assessment.

558 **Table 3**

559 Percentage match and deviation between the measured k and the predicted k' for 18 selected data points
 560 out of the total 116

CSAMT data points (selected)			Drilling data			%Matching	Difference
CSAMT sounding number	Resistivity (Ωm)	Predicted k' (mD) using Eq. (3)	Borehole name	Depth (m)	Measured k (mD)	k' vs k	between k' and k
P1-5	392	7.0	BH-1	10	9.6	73	2.6
P1-5	515	5.5	BH-1	40	8.7	63	3.2
P1-5	1080	1.8	BH-1	170	1.8	100	0.0
P1-9	669	4.0	BH-2	20	5.0	80	1.0
P1-9	863	2.7	BH-2	60	3.5	77	0.8
P1-9	1354	1.02	BH-2	185	1.2	85	0.18
P2-3	2187	0.2	BH-3	10	0.3	67	0.1
P2-3	2988	0.04	BH-3	85	0.1	40	0.06
P2-3	4765	0.003	BH-3	200	0.01	30	0.007
P6-1	50	13.9	BH-4	15	19.9	70	6.0
P6-1	200	10.3	BH-4	100	12.0	86	1.7
P6-1	348	7.7	BH-4	180	9.9	78	2.2
P3-15	792	3.3	BH-5	30	4.1	80	0.8
P3-15	1157	1.5	BH-5	135	1.6	94	0.1
P3-15	1412	0.91	BH-5	200	1.07	85	0.16
P3-21	165	11.1	BH-6	45	18.2	61	7.1
P3-21	708	3.7	BH-6	165	5.0	74	1.3
P3-21	846	2.8	BH-6	180	2.0	71	0.8

561

562 **4 Discussion**

563 **4.1 Scalable geophysical approach for deep groundwater modeling**

564 The integration of geophysics into groundwater studies provides an efficient and scalable
565 substitute for borehole-based methods, especially in deep and geologically complex terrains.
566 While boreholes provide direct k data, their use is limited by cost, logistics, and sparse coverage.
567 Our study presents a robust framework for 2D and 3D k modeling beyond 1 km depth by
568 integrating CSAMT with borehole data in a lithologically diverse setting. This approach
569 addresses key challenges in areas with limited surface water and low- k granite near the surface,
570 revealing deeper fractured zones with higher groundwater potential in granite, hornstone, and
571 sandstone. These deep aquifer insights support China's national water security strategies and
572 inform sustainable groundwater management under climate stress.

573 **4.2 Ensuring data quality and model reliability**

574 To minimize uncertainty and enhance accuracy, we implemented a rigorous workflow
575 throughout data acquisition, processing, inversion, and modeling. For CSAMT, this included
576 careful survey planning, optimized electrode configurations, and the application of advanced
577 filtering and static shift corrections. Inversion was guided by multidimensional modeling
578 constrained by borehole-derived a priori information, improving resolution and mitigating non-
579 uniqueness. Permeability measurements were obtained under controlled laboratory conditions
580 using high-quality, undisturbed core samples from six boreholes, reducing discrepancies between
581 laboratory and field scales. These measures, together with integrated lithological data, enabled

582 the development of a robust k model suitable for reliable groundwater assessment across the
583 study area.

584 **4.3 Comparative advantages of CSAMT for deep hard rock aquifer characterization**

585 CSAMT, developed in the 1970s, remains uniquely valuable for deep subsurface exploration,
586 particularly in resistive and fractured hard rock environments. Its ability to image at
587 intermediate-to-deep depths (hundreds to over a thousand meters) with relatively high resolution
588 and controlled signal strength enhances its ability to delineate lithological contacts and fluid-
589 bearing formations where other resistivity methods (VES and ERT) may fall short. While
590 electromagnetic methods such as MT and TDEM are also capable of probing deep subsurface
591 structures, achieving comparable results in similarly complex hard rock settings presents notable
592 challenges. MT, which relies on natural variations in electromagnetic fields, can reach even
593 greater depths than CSAMT and has been successfully applied in regional-scale hydrogeological
594 investigations, such as identifying deep groundwater circulation paths in mountain systems
595 (Jiang et al., 2014) and tracing flow systems that recharge lowland aquifers (Gonzalez-Duque et
596 al., 2024).

597 As summarized in Table 1, MT provides exceptional penetration (tens of kilometers) but
598 has reduced resolution in the upper crust and is highly sensitive to cultural noise, limiting its
599 suitability for detailed k -modeling at the site scale. TDEM, while rapid and effective for
600 intermediate depths, suffers loss of sensitivity in highly resistive formations, making it less
601 effective for fractured granite and hornstone settings. In contrast, CSAMT's controlled-source
602 design and strong immunity to cultural noise provide a balance of depth penetration and
603 resolution well-suited for site-specific groundwater studies in hard rock terrains.

604 Thus, the comparative analysis (Table 1) underscores why CSAMT is the most
605 appropriate method for this study: it bridges the gap between large-scale regional techniques
606 (MT, TDEM) and shallow, high-resolution methods (VES, ERT), enabling robust 2D and 3D
607 hydrogeophysical modeling essential for evaluating deep aquifer potential.

608 **4.4 Calibrated resistivity thresholds for lithological and hydraulic discrimination**

609 We developed a robust empirical relationship between resistivity and k using 116 co-located data
610 pairs, 62 from granite, 31 from sandstone, and 23 from hornstone, spanning 35–4,765 Ωm and
611 0.01–19.9 mD, respectively. The strong correlation ($R^2 = 0.96$) ensures reliable k prediction and
612 minimizes lithological bias. The lithological classification derived from the resistivity–
613 permeability relationship in this study is both geologically plausible and empirically supported
614 by borehole data and field observations. Specifically, granite showed high resistivity ($>700 \Omega\text{m}$)
615 and low k (0–5 mD), hornstone had intermediate resistivity (350–700 Ωm) and moderate k (5–
616 10 mD), and sandstone was marked by low resistivity ($<350 \Omega\text{m}$) and higher k (10–20 mD).
617 These ranges align with the distinct hydrogeological behaviors of each lithology under the site-
618 specific structural and mineralogical conditions. The resistivity thresholds were selected through
619 an integrated approach combining lithological logs from boreholes, established empirical
620 resistivity values reported in the literature, and the geoelectrical contrasts identified in CSAMT
621 profiles. For instance, the high resistivity of granite reflects its dense, low-porosity matrix and
622 limited fluid content, whereas the lower resistivity of sandstone and hornstone corresponds to
623 increased pore connectivity and higher saturation, often associated with structural features or
624 thermal alteration. To ensure robust classification, the resistivity thresholds were calibrated using
625 co-located borehole observations from multiple calibration sites and iteratively refined to
626 maximize agreement between observed lithology and the modeled resistivity–permeability

627 domains. While we acknowledge that resistivity can vary within a given lithology due to
628 localized factors such as fluid saturation, mineral alteration, or fracture density, sensitivity
629 analyses indicated that moderate adjustments to the threshold values had minimal impact on the
630 overall lithological classification or the interpretation of k trends. This suggests that the chosen
631 thresholds are well-suited to the structurally complex Jinji area. Nevertheless, we emphasize that
632 these resistivity–permeability associations are localized and should be recalibrated to account for
633 site-specific conditions before use elsewhere. Although site-specific, the approach demonstrates
634 how minimal calibration data can support high-resolution 2D/3D k modeling in data-scarce
635 settings. Future studies could benefit from probabilistic classification schemes or machine
636 learning approaches to further refine lithological mapping in geologically heterogeneous terrains.

637 **4.5 Impact of lithological and measurement variability on the resistivity–permeability** 638 **relationship**

639 The fitted relationship between resistivity and k , as illustrated in Fig. 5, is shaped by several
640 factors, including the geological setting, lithological heterogeneity, data distribution, and the
641 accuracy of both measurements. The broad dynamic range in our dataset provides a strong basis
642 for identifying trends across the three dominant lithologies: sandstone, granite, and hornstone.
643 This broad range is especially beneficial for resolving low- k formations such as granite, where k
644 remains uniformly low and shows minimal fluctuation. In these settings, even large shifts in
645 resistivity translate to relatively small changes in k , resulting in a gently declining inverse
646 relationship. In contrast, at lower resistivity values (e.g., $<1,000 \Omega\text{m}$) where k exceeds 2 mD,
647 small resistivity shifts result in larger changes in k , leading to a more scattered and nonlinear
648 correlation. This pattern is geologically realistic and reflects the inherent variability of fractured
649 and porous zones in complex lithologies.

650 **4.6 Model validation and predictive reliability**

651 Matching between measured and predicted permeability (k vs. k') was also rigorously validated
652 (Table 3). Among 18 selected points from boreholes, 10 showed a difference of less than 1 mD,
653 with only two exceeding 4 mD. Despite minor deviations, all points were accurately classified by
654 lithology. This confirms the empirical model's reliability and its utility for regional-scale k
655 prediction, even in areas lacking direct measurements. The geophysical model effectively
656 compensates for sparse drilling data, offering a scalable and cost-effective tool for
657 hydrogeological evaluation in hard rock terrains.

658 **4.7 Limited and shallow borehole calibration**

659 A key limitation of this study lies in the depth extent of the calibration dataset. The empirical
660 resistivity–permeability relationship was developed using 116 core samples from six boreholes,
661 all restricted to depths between 0 and 200 m. Extrapolating this relationship to 1300 m depth
662 introduces uncertainty, as no direct calibration exists at greater depths. To address this limitation,
663 we incorporated a probabilistic modeling framework that quantifies the increase in uncertainty
664 with depth. The model results (Fig. 13) clearly illustrate that while near-surface permeability
665 estimates are relatively well constrained, the confidence intervals expand significantly beyond
666 ~200 m due to the lack of direct sampling.

667 Future work should therefore prioritize the acquisition of deep borehole data (>500 m),
668 including core sampling, hydraulic pumping tests, and packer testing, to directly validate the
669 extrapolated permeability values. In addition, the integration of advanced downhole geophysical
670 logging with geostatistical and probabilistic approaches will provide stronger constraints on
671 subsurface heterogeneity at depth. Such efforts will be essential to improve confidence in deep

672 permeability predictions, reduce geological uncertainty, and enhance the reliability of
673 groundwater resource assessments in complex crystalline terrains.

674 **4.8 Choice of core-based permeability measurements versus pumping tests**

675 Although pumping tests are widely regarded as the standard method for estimating aquifer
676 permeability (k), they provide only bulk, large-scale averages of hydraulic conductivity over the
677 tested interval. Such measurements are useful for assessing overall transmissivity but lack the
678 spatial resolution required for detailed 2D or 3D geophysical modeling, where localized contrasts
679 in hydraulic properties are critical. The objective of this study was to capture subsurface
680 heterogeneity at scales compatible with CSAMT-derived resistivity. For this purpose, point-
681 specific k measurements were necessary to ensure that calibration data reflected the same
682 resolution and spatial variability represented in the geophysical models. Core samples, analyzed
683 at discrete depths, offered this localized control and provided a closer match to the spatial scale
684 of CSAMT blocks. Therefore, core-derived k values were used in lieu of pumping tests. While
685 this approach inevitably shifts the focus from bulk aquifer transmissivity to matrix- and fracture-
686 scale variability, it ensures that the calibration dataset is scale-compatible with resistivity
687 measurements, thereby improving the reliability of the empirical k - ρ relationship and supporting
688 more accurate heterogeneity mapping in crystalline terrains.

689 **4.9 Scale effects in permeability estimation**

690 While core plug measurements and CSAMT-derived resistivity are broadly compatible for
691 establishing an empirical k - ρ relationship, it is important to acknowledge the differences in
692 sampling scale. Core-derived permeability (k) values, measured on centimeter-scale samples,
693 largely capture matrix properties of the rock. These may underestimate flow capacity where

694 nearby fractures or heterogeneities are missed. In contrast, CSAMT inversions, with an effective
695 resolution of $\sim 50 \times 50$ m, represent a bulk effective property that integrates both matrix and
696 fracture contributions across larger volumes.

697 This scale difference provides a natural explanation for the scatter observed in the k - ρ
698 dataset (Fig. 5). For example, a core extracted from intact granite may record low k , while the
699 corresponding CSAMT block encompasses a fracture corridor that increases the effective k .
700 Conversely, a core intersecting a fracture may yield anomalously high k compared to the
701 surrounding bulk medium resolved by CSAMT. Thus, while the fine-scale core data were
702 essential for establishing point-specific calibration with resistivity values, the observed scatter
703 reflects the complementary strengths of the two approaches: core testing constrains intrinsic rock
704 matrix properties, and CSAMT captures fracture-controlled heterogeneity and connectivity at the
705 field scale. Together, they provide a more robust characterization of hydraulic behavior than
706 either method alone. Future work should strengthen this multi-scale integration by including
707 intermediate-scale datasets such as borehole geophysics and aquifer-scale pumping tests. Such
708 efforts would further bridge the gap between matrix-scale and bulk-scale measurements,
709 reducing uncertainty in k modeling for complex crystalline terrains.

710 **4.10 Inflection in the resistivity–permeability relationship: a depth analogue**

711 The empirical resistivity–permeability (k - ρ) relationship developed in this study exhibits a sharp
712 decline in k with increasing resistivity and a clear inflection near 1,000 Ωm . This mirrors classic
713 depth–permeability (k - z) trends (e.g., Manning and Ingebritsen, 1999; Saar and Manga, 2004;
714 Ingebritsen and Manning, 2010), where k decreases exponentially at shallow depths and follows
715 a power-law pattern deeper down. However, unlike those models that use depth alone, our
716 resistivity-based approach captures additional controls such as lithology, porosity, fluid content,

717 and fracturing, making it a more localized and physically representative proxy, especially in
718 heterogeneous hard rock settings.

719 Depth was considered but not used as the primary variable due to strong lateral variations
720 in resistivity and k caused by geological complexity. For instance, in the Jinji area, surface
721 granite shows high resistivity and low k , consistent with standard crustal profiles. However,
722 deeper hornstone and sandstone units exhibit lower resistivity and higher k , contrary to typical
723 depth trends, likely due to localized faulting, thermal alteration, and contact metamorphism that
724 enhance fracture connectivity. The resemblance between our k - ρ curve and established k - z
725 models reinforces its physical validity. The observed transition near 1,000 Ωm may reflect a shift
726 from conductive, fractured zones to compact, resistive rock masses. While hybrid models
727 incorporating depth may be useful in future work, our resistivity-based method provides a more
728 reliable and site-specific approach for k estimation in structurally complex terrains.

729 **4.11 Salinity effects and uncertainty in deep fluid properties**

730 The influence of factors beyond lithology, particularly groundwater salinity, on CSAMT-derived
731 resistivity warrants consideration. Electrical resistivity is inherently sensitive to porosity, fracture
732 density, mineral alteration, fluid saturation, and salinity. In this study, k calibration was based on
733 core samples from 0–200 m depths across six boreholes. While this limits direct calibration at
734 greater depths, hydrochemical data from the Geological Survey of China, spanning 800–1,000 m
735 depth, consistently indicate fresh groundwater, suggesting salinity is not the cause of deeper low-
736 resistivity zones. We interpret these zones, especially in sandstone and hornstone, as reflecting
737 high saturation and pore connectivity rather than saline fluids. This is further supported by the

738 absence of resistivity anomalies typically associated with brackish water, and the strong
739 alignment between resistivity, k , and lithological boundaries.

740 However, because no fluid data are available below 1 km, the role of salinity cannot be
741 entirely excluded, representing a key assumption and limitation of this study. A sensitivity
742 analysis indicates that if fluid resistivity (ρ_f) were halved due to salinity, the apparent formation
743 resistivity (ρ) would decrease by ~50%. Substituting this reduced resistivity into our resistivity–
744 permeability relationship (Eq. 3) yields higher permeability (k) values, as k increases
745 exponentially with decreasing ρ . Specifically, halving ρ_f would increase inferred k by
746 approximately a factor of 2 at 1000 Ωm , 7 at 2000 Ωm , and 18 at 3000 Ωm . These results
747 demonstrate that salinity effects are modest at shallow depths but may become significant at
748 greater depths. Future investigations should therefore incorporate deep borehole sampling, fluid
749 logging, and hydrochemical analyses to directly constrain fluid resistivity and reduce uncertainty
750 in k extrapolation.

751 **4.12 Uncertainty from model extrapolation and edge effects**

752 The 3D permeability (k) model was constructed by interpolating between 2D CSAMT inversion
753 profiles calibrated with borehole-derived k values from six reference locations. Given the
754 limitations in survey geometry and computational cost, full 3D inversion of the resistivity data
755 was not feasible. Instead, we implemented a geostatistical framework using ordinary kriging,
756 which integrated cross-sectional profiles and applied the resistivity–permeability relationship
757 across the model volume. The interpolation was guided by variogram models tuned to reflect the
758 spatial continuity of lithological units and constrained by borehole control points, thereby
759 maintaining geological consistency. While this approach provides a volumetric representation of

760 k that highlights the distribution of permeable zones, its reliability is scale- and data-density
761 dependent. The model is most robust in the central areas where CSAMT lines intersect and are
762 directly supported by borehole data. In contrast, reliability diminishes in regions between widely
763 spaced profiles and toward the model edges and corners, where no direct constraints exist.
764 Sensitivity analyses, based on alternative variogram structures and comparisons with inverse
765 distance weighting, consistently revealed greater variability and uncertainty in these peripheral
766 zones.

767 To address this, uncertainty contours were added to Figs. 10 and 11, delineating areas of
768 higher and lower confidence. The black dots marking borehole and survey line positions serve as
769 reference anchors, making it clear that interpolation quality decreases with increasing distance
770 from these control points. As such, interpretations in boundary regions should be treated with
771 caution, particularly where model predictions extend beyond the convex hull of available data.
772 We emphasize that the current model provides a reliable first-order framework for k distribution
773 in the study area, but future improvements should prioritize denser CSAMT line coverage and,
774 where feasible, the use of full 3D inversion techniques. Such approaches would better capture
775 lateral continuity, minimize edge effects, and enhance confidence in the extrapolated 3D
776 structure.

777 **4.13 Limitations of storage characterization**

778 A complete aquifer assessment requires evaluation of both permeability (k) and storage
779 parameters such as storativity, specific yield, and specific storage. This study focused primarily
780 on delineating spatial variations in k , referred to here as “water-bearing capacity,” using
781 CSAMT-derived resistivity calibrated with borehole data. While this approach provides valuable

782 insights into transmissivity and flow potential, it does not directly constrain aquifer storage
783 capacity.

784 Due to the absence of deep pumping tests and detailed formation logs, storage parameters
785 could not be quantified. Instead, our interpretations rely on qualitative geological and
786 geophysical inference. Permeable units like sandstone and hornstone likely possess higher
787 porosity due to their granular textures and fracture networks, unlike the denser granite. This is
788 supported by groundwater level data from six boreholes and regional water table records, which
789 indicate aquifers in fractured, low-resistivity zones. These zones align spatially with permeable
790 features in both CSAMT/ k models and borehole data.

791 We acknowledge that the current study characterizes relative transmissivity rather than
792 absolute storage capacity, representing a key limitation. Future work should therefore integrate
793 porosity and storage characterization through deep borehole testing, in-situ hydrochemical and
794 geophysical logging (e.g., nuclear magnetic resonance), and aquifer hydraulic analysis to provide
795 a more comprehensive basis for groundwater resource evaluation in complex hard rock terrains.

796 **4.14 Optimizing borehole placement for CSAMT calibration**

797 Borehole placement in this study was strategically guided by geological mapping, hydrological
798 relevance, and preliminary geophysical data to ensure representative coverage of key lithologies
799 and structures. These boreholes served both to calibrate resistivity–permeability relationships
800 and to validate the CSAMT-derived k models. While there’s no fixed number of required
801 boreholes, our results show that a small but well-distributed set across major lithological and
802 structural zones yields reliable model performance. A leave-one-out validation confirmed that
803 the model maintains coherent spatial trends, though with slightly reduced accuracy in

804 geologically complex areas. This highlights both the importance of strategic calibration point
805 distribution and the robustness of the CSAMT-based approach, even with limited borehole data.
806 Future efforts could improve efficiency by adapting borehole placement based on preliminary
807 CSAMT results, optimizing both calibration and cost.

808 **4.15 Rationale for variable CSAMT profile extents**

809 The variation in CSAMT profile lengths reflects site-specific logistical and geological
810 constraints encountered during field deployment. Factors such as terrain accessibility,
811 infrastructure (e.g., roads, buildings), and the need to capture key geological features (e.g., faults,
812 lithological boundaries) influenced the extent of each profile. In some cases, shorter profiles
813 were required due to rugged topography or land access limitations, while longer profiles were
814 employed where feasible to ensure adequate coverage across broader structural domains. Despite
815 the variation in length, all profiles were designed to achieve sufficient depth penetration and
816 resolution for reliable resistivity–permeability modeling, as validated through borehole
817 calibration.

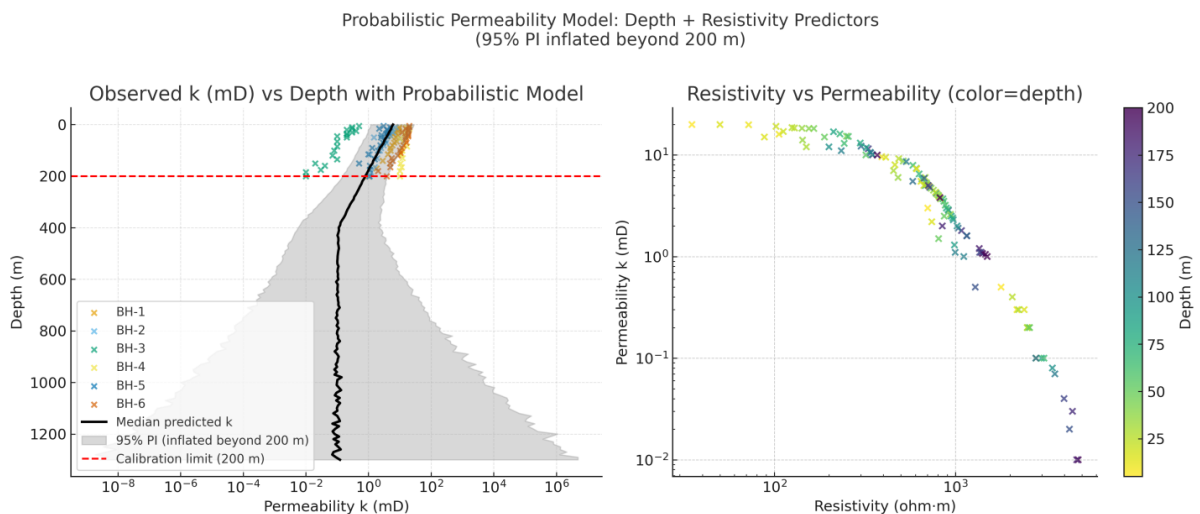
818 **4.16 Addressing the borehole–CSAMT depth discrepancy**

819 Although the borehole data used for calibration were limited to depths of 0–200 m, this interval
820 encompasses key lithological units, granite, hornstone, and sandstone, and captures a
821 representative range of resistivity and k conditions. These near-surface measurements provided a
822 robust basis for developing the empirical resistivity–permeability (k – ρ) relationship, which was
823 subsequently applied across the full depth range of the CSAMT profiles (~1300 m). While direct
824 validation at greater depths is not currently possible due to the absence of deep borehole data, the

825 extrapolation of the calibrated model is supported by consistent geological structure,
 826 hydrochemical data, and stratigraphic continuity reported by the Geological Survey of China
 827 down to ~1000 m. Furthermore, strong spatial alignment between resistivity, inferred k , and
 828 mapped lithological boundaries lends confidence to the model's deeper projections. We
 829 acknowledge this depth mismatch as a limitation, but emphasize that the approach enables
 830 meaningful k estimation in data-scarce regions. Future studies incorporating deep drilling and in-
 831 situ petrophysical logging will be essential to further refine model accuracy at greater depths.

832 4.17 Ground-truthing CSAMT with regional geological frameworks

833 Our results show strong agreement with regional geological and hydrogeological data from local
 834 and national surveys, confirming the reliability of the integrated CSAMT–borehole approach.
 835 This alignment supports the method’s scientific validity and scalability for k estimation in
 836 structurally complex, data-scarce settings. While grounded in established geophysical principles,
 837 the strength of this study lies in its site-specific integration of deep k modeling, field validation,
 838 and empirical calibration. Overall, the findings highlight CSAMT’s potential as a practical tool
 839 for deep groundwater exploration and sustainable resource management.



840

841 **Fig. 13.** Probabilistic permeability–depth model based on resistivity–permeability calibration from 116
842 borehole samples (0–200 m). The extrapolation to 1300 m shows increasing uncertainty with depth due to
843 limited calibration data.

844 **5 Conclusions**

845 This study introduces a novel, non-invasive methodology for deep groundwater investigation
846 using CSAMT, applied for indirect estimation of 2D and 3D k distributions in complex hard rock
847 terrains at depths reaching 1300 m. Conventional borehole drilling remains indispensable for
848 direct hydraulic parameter evaluation, but its high cost and limited coverage restrict broader
849 applicability. Our approach combines borehole calibration with CSAMT resistivity to establish
850 an empirical k – ρ relationship, enabling the construction of spatially continuous hydrogeological
851 models that extend beyond the reach of direct sampling.

852 It is important to note that the empirical relationship (Eq. 3) derived in this study is site-
853 specific to the Jinji region’s geological and hydrogeochemical conditions. Its constants should
854 not be generalized to other regions without new calibration data. The key contribution of this
855 work is therefore the methodology, a workflow for integrating CSAMT with borehole
856 calibration, rather than the specific coefficients of the empirical equation. The resulting
857 permeability models align well with lithological boundaries, revealing low- k granite zones (>700
858 Ωm , 0–5 mD) and high- k sandstone zones (<350 Ωm , 10–20 mD). Promising groundwater
859 targets were identified below 700 m in central regions and around granite–sediment contacts,
860 extending to depths of ~ 1300 m. While these results demonstrate the power of CSAMT for deep
861 groundwater assessment, they remain dependent on the availability and quality of borehole data
862 for calibration.

863 Future work should emphasize deep borehole validation, probabilistic modeling, and
864 multi-scale integration to reduce uncertainty and improve confidence in permeability predictions.
865 By coupling CSAMT with hydrochemical, porosity, and advanced logging data, this approach
866 can evolve into a robust and transferable framework for groundwater assessment in complex
867 hard rock terrains, while acknowledging inherent site-specific limitations.

868 **Code availability**

869 Software application or custom code supports the published claims and complies with field
870 standards

871 **Data availability**

872 Data available on request from the corresponding author

873 **Author contributions**

874 MH conceptualized the research goals and developed the methodology. MH and LS found the
875 funding for the project. MH developed the code and prepared its visualization, and LS provided
876 programming support and analysis tools. MH prepared the original draft.

877 **Declaration of competing interest**

878 The authors declare that they have no conflict of interest.

879 **Acknowledgements**

880 The authors gratefully acknowledge the support provided by the State Key Laboratory of
881 Mountain Hazards and Engineering Resilience, Institute of Mountain Hazards and Environment,

882 Chinese Academy of Sciences, and the China-Pakistan Joint Research Center on Earth Sciences,
883 CAS-HEC, Islamabad, Pakistan.

884 **Financial support**

885 This research was financially supported by the National Natural Science Foundation of China
886 (Grant No. U22A20603), the International Science and Technology Cooperation Program of
887 Shanghai Cooperation Organization, Science and Technology Department, Xinjiang, China
888 (Grant No. E202301005), and the National Natural Science Foundation of China's Research
889 Fund for International Young Scientists (RFIS-I) (Grant No. 42350410442).

890 **References**

- 891 1. Abbas, M., Deparis, J., Isch, A., Mallet, C., Jodry, C., Azaroual, M., Abbar, B., and
892 Baltassat, J.M.: Hydrogeophysical characterization and determination of petrophysical
893 parameters by integrating geophysical and hydrogeological data at the limestone vadose
894 zone of the Beauce aquifer, *Journal of Hydrology*, 615, 128725, 2022.
895 <https://doi.org/10.1016/j.jhydrol.2022.128725>.
- 896 2. Allègre, V., Brodsky, E.E., Xue, L., Nale, S.M., Parker, B.L., and Cherry, J.A.: Using
897 earth-tide induced water pressure changes to measure in situ permeability: A comparison
898 with long-term pumping tests, *Water Resour. Res.*, 52(4), 3113–3126, 2016.
899 <https://doi.org/10.1002/2015WR017346>.
- 900 3. Amiotte Suchet, P., Probst, J.L., and Ludwig, W.: Worldwide distribution of continental
901 rock lithology: Implications for the atmospheric/ soil CO₂ uptake by continental
902 weathering and alkalinity river transport to the oceans, *Glob Biogeochem Cycles*, 17,
903 1038, 2003. <https://doi.org/10.1029/2002GB001891>.

- 904 4. Archie, G.E.: The electrical resistivity log as an aid in determining some reservoir
905 characteristics, Transactions of the AIME, 146(1), 54–62, 1942.
906 <https://doi.org/10.2118/942054-G>.
- 907 5. Asfahani, J.: Estimation of the hydraulic parameters by using an alternative vertical
908 electrical sounding technique: case study from semiarid Khanasser valley region
909 Northern Syria, Acta Geophys, 71, 997–1013, 2023. [https://doi.org/10.1007/s11600-022-](https://doi.org/10.1007/s11600-022-00926-0)
910 [00926-0](https://doi.org/10.1007/s11600-022-00926-0).
- 911 6. ASTM.: Standard Test Methods for Measurement of Hydraulic Conductivity of Saturated
912 Porous Materials Using a Flexible Wall Permeameter (ASTM D5084-21), ASTM
913 International, 2021. DOI: 10.1520/D5084-21.
- 914 7. Bauer-Gottwein, P., Gondwe, B.N., Christiansen, L., Herckenrath, D., Kgotlhang, L., and
915 Zimmermann, S.: Hydrogeophysical exploration of three-dimensional salinity anomalies
916 with the time domain electromagnetic method (TDEM), J. Hydrol., 380(3–4), 318–329,
917 2010. <https://doi.org/10.1016/j.jhydrol.2009.11.007>.
- 918 8. Bear, J.: Dynamics of Fluids in Porous Media. New York: American Elsevier Publishing
919 Company, 1972.
- 920 9. Binley, A., Cassiani, G., and Deiana, R.: Hydrogeophysics: opportunities and challenges,
921 Bollettino Di Geofisica Teorica Ed Applicata, 51(4), 267–287, 2010. [Online]. Available:
922 [http://www.scopus.com/inward/record.url?eid=2-s2.0-](http://www.scopus.com/inward/record.url?eid=2-s2.0-78650438167&partnerID=40&md5=96e14979c82f4b23e8fed0ac0140e7db)
923 [78650438167&partnerID=40&md5=96e14979c82f4b23e8fed0ac0140e7db](http://www.scopus.com/inward/record.url?eid=2-s2.0-78650438167&partnerID=40&md5=96e14979c82f4b23e8fed0ac0140e7db).
- 924 10. Binley, A., Hubbard, S.S., Huisman, J.A., Revil, A., Robinson, D.A., Singha, K., and
925 Slater, L.D.: The emergence of hydrogeophysics for improved understanding of

- 926 subsurface processes over multiple scales, *Water Resources Research*, 51(6), 3837–3866,
927 2015. <https://doi.org/10.1002/2015WR017016>.
- 928 11. Borah, U.K., and Patro, P.K.: Estimation of the depth of investigation in the
929 magnetotelluric method from the phase, *Geophysics*, 84 (6), E377–E385, 2019.
930 <https://doi.org/10.1190/geo2018-0124.1>.
- 931 12. Brace, W.F., Walsh, J.B., and Frangos, W.T.: Permeability of granite under high pressure,
932 *Journal of Geophysical Research*, 73(6), 2225–2236, 1968.
933 <https://doi.org/10.1029/JB073i006p02225>.
- 934 13. Cagniard, L.: Basic theory of the magneto-telluric method of geophysical
935 prospecting, *Geophysics*, 18 (3), 605–635, 1953. <https://doi.org/10.1190/1.1437915>.
- 936 14. Carbillet, L., Griffiths, L., Heap, M.J., Duwiquet, H., Baud, P., Violay, M.E.S., Reuschlé,
937 T., and Guillou-Frottier, L.: The Influence of Micro- and Macrocracks on the
938 Permeability of Granite, *Rock Mech Rock Eng*, 58, 1361–1378, 2024.
939 <https://doi.org/10.1007/s00603-024-04174-0>.
- 940 15. Chapuis, R.P., and Aubertin, M.: Predicting the Coefficient of Permeability of Soils
941 Using the Kozeny-Carman Equation. *E ´cole Polytech. Montre ´al*, 2003, [Online].
942 Available: <http://publications.polymtl.ca/2605/>
- 943 16. Condon, L.E., Markovich, K.H., Kelleher, C.A., McDonnell, J.J., Ferguson, G., and
944 McIntosh, J.C.: Where Is the Bottom of a Watershed? *Water Resources Research*, 56(3),
945 e2019WR026010, 2020. <https://doi.org/10.1029/2019WR026010>.
- 946 17. Daily, W., Ramirez, A., LaBrecque, D., and Nitao, J.: Electrical resistivity tomography of
947 vadose water movement, *Water Resources Research*, 28(5), 1429–1442, 1992.
948 <https://doi.org/10.1029/91WR03087>.

- 949 18. DallaValle, J.M.: Flow of Gases through Porous Media. P. C. Carman, Academic Press,
950 New York; Butterworths, London, 1956. 182 pp. Illus, 1956.
951 <https://www.science.org/doi/10.1126/science.124.3234.1254.b>.
- 952 19. Dell'Oca, A., Guadagnini, A., and Riva, M.: Interpretation of multi-scale permeability
953 data through an information theory perspective, *Hydrol. Earth Syst. Sci.*, 24, 3097–3109,
954 2020. <https://doi.org/10.5194/hess-24-3097-2020>.
- 955 20. Dewandel, B., Lachassagne, P., Wyns, R., Maréchal, J.C., and Krishnamurthy, N.S.: A
956 generalized 3-D geological and hydrogeological conceptual model of granite aquifers
957 controlled by single or multiphase weathering, *Journal of Hydrology*, 330(1–2), 260–284,
958 2006. <https://doi.org/10.1016/j.jhydrol.2006.03.026>.
- 959 21. Di, Q., Fu, C., An, Z., Wang, R., Wang, G., Wang, M., Qi, S., and Liang, P.: An
960 application of CSAMT for detecting weak geological structures near the deeply buried
961 long tunnel of the Shijiazhuang-Taiyuan passenger railway line in the Taihang Mountains,
962 *Engineering Geology*, 268, 105517, 2020. <https://doi.org/10.1016/j.enggeo.2020.105517>.
- 963 22. Esmailpour, M., Ghanbarian, B., Sousa, R., Peter, R., and King, P.R.: Estimating
964 Permeability and Its Scale Dependence at Pore Scale Using Renormalization Group
965 Theory, *Water Resources Research*, 59 (5), e2022WR033462, 2023.
966 <https://doi.org/10.1029/2022WR033462>.
- 967 23. Ferguson, G., McIntosh, J.C., Jasechko, S., Kim, J.H., Famiglietti, J.S., and McDonnell,
968 J.J.: Groundwater deeper than 500 m contributes less than 0.1% of global river
969 discharge, *Communication Earth and Environment*, 4, 48, 2023.
970 <https://doi.org/10.1038/s43247-023-00697-6>.

- 971 24. Fernando, A., and Pacheco, L.: Regional groundwater flow in hard rocks, *Science of the*
972 *Total Environment*, 506–507, 182–195, 2015.
973 <https://doi.org/10.1016/j.scitotenv.2014.11.008>.
- 974 25. Ferré, T., Bentley, L., Binley, A., Linde, N., Kemna, A., Singha, K., Holliger,
975 k., Huisman, J.A., Minsley, B.: Critical Steps for the Continuing Advancement of
976 Hydrogeophysics. *Eos, Transactions American Geophysical Union*, 90(23), 200, 2009.
977 <https://doi.org/10.1029/2009EO230004>.
- 978 26. Fiandaca, G., Maurya, P.K., Balbarini, N., Hördt, A., Christiansen, A.V., Foged, N.,
979 Bjerg, P.L., and Auken, E.: Permeability estimation directly from logging-while-drilling
980 induced polarization data, *Water Resources Research*, 54, 2851–2870,
981 2018. <https://doi.org/10.1002/2017WR022411>.
- 982 27. Fu, C., Di, Q., and An, Z.: Application of the CSAMT method to groundwater
983 exploration in a metropolitan environment, *Geophysics*, 78 (5), B201–B209, 2013.
984 <https://doi.org/10.1190/geo2012-0533.1>.
- 985 28. Fusheng, G., Haiyan, Y., Zengqian, H., Zhichun, W., Ziyu, L., Guocan, W., Linfu, X., Ye,
986 G., and Wanpeng, Z.: Structural setting of the Zoujiashan-Julong'an region, Xiangshan
987 volcanic basin, China, interpreted from modern CSAMT data, *Ore Geology Reviews*, 150,
988 105180, 2022. <https://doi.org/10.1016/j.oregeorev.2022.105180>.
- 989 29. Gerke, H.H., Dusek, J., and Vogel, T.: Mass transfer effects in 2-D dual-permeability
990 modeling of field preferential bromide leaching with drain effluent, *Hydrol. Earth Syst.*
991 *Sci. Discuss.*, 8, 5917–5967, 2011. <https://doi.org/10.5194/hessd-8-5917-2011>.
- 992 30. Gleeson, T., Moosdorf, N., Hartmann, J., and van Beek, L.P.H.: A glimpse beneath
993 earth's surface: Global hydrogeology maps (GLHYMPS) of permeability and porosity,

- 994 Geophysical Research Letters, 41(11), 3891–3898, 2014.
995 <https://doi.org/10.1002/2014GL059856>.
- 996 31. Glover, P.W.J.: Geophysical properties of the near surface Earth: electrical properties,
997 Treatise on Geophysics, 11, 89–137, 2015. [https://doi.org/10.1016/B978-0-444-53802-](https://doi.org/10.1016/B978-0-444-53802-4.00189-5)
998 [4.00189-5](https://doi.org/10.1016/B978-0-444-53802-4.00189-5).
- 999 32. Glover, P.W.J.: What is the cementation exponent? A new interpretation, The Leading
1000 Edge, 28(1), 82–85, 2009. <https://doi.org/10.1190/1.3064150>.
- 1001 33. Gonzalez-Duque, D., Gomez-Velez, J.D., Person, M.A., Kelley, S., Key, K., and Lucero,
1002 D.: Groundwater Circulation Within the Mountain Block: Combining Flow and Transport
1003 Models With Magnetotelluric Observations to Untangle Its Nested Nature, Water
1004 Resources Research, 60(4), e2023WR035906, 2024.
1005 <https://doi.org/10.1029/2023WR035906>.
- 1006 34. Hasan, M., and Shang, Y.: Geophysical evaluation of geological model uncertainty for
1007 infrastructure design and groundwater assessments, Engineering Geology, 299, 106560,
1008 2022. <https://doi.org/10.1016/j.enggeo.2022.106560>.
- 1009 35. Hasan, M., Shang, Y., Jin, W., and Akhter, G.: Estimation of hydraulic parameters in a
1010 hard rock aquifer using integrated surface geoelectrical method and pumping test data in
1011 southeast Guangdong China, Geosci J, 25 (2), 223–242, 2021.
1012 <https://doi.org/10.1007/s12303-020-0018-7>.
- 1013 36. Hasan, M., Su, L., Cui, P., and Shang, Y.: Development of deep-underground
1014 engineering structures via 2D and 3D RQD prediction using non-invasive
1015 CSAMT, Scientific Reports, 15, 1403, 2025. <https://doi.org/10.1038/s41598-025-85626-7>.

- 1016 37. Herckenrath, D., Auken, E., Christiansen, L., Behroozmand, A.A., and Bauer - Gottwein,
1017 P.: Coupled hydrogeophysical inversion using time-lapse magnetic resonance sounding
1018 and time-lapse gravity data for hydraulic aquifer testing: Will it work in practice? *Water*
1019 *Resources Research*, 48(1), W01539, 2012. <https://doi.org/10.1029/2011WR010411>.
- 1020 38. Herckenrath, D., Odlum, N., Nenna, V., Knight, R., Auken, E., and Bauer - Gottwein, P.:
1021 Calibrating a Salt Water Intrusion Model with Time-Domain Electromagnetic Data,
1022 *Groundwater*, 51(3), 385–397, 2013. <https://doi.org/10.1111/j.1745-6584.2012.00974.x>.
- 1023 39. Hinnell, A.C., Ferré, T.P.A., Vrugt, J.A., Huisman, J.A., Moysey, S., Rings, J., and
1024 Kowalsky, M.B.: Improved extraction of hydrologic information from geophysical data
1025 through coupled hydrogeophysical inversion, *Water Resources Research*, 46(4), W00D40,
1026 2010. <https://doi.org/10.1029/2008WR007060>.
- 1027 40. Hu, X.Y., Peng, R.H., Wu, G.J., Wang, W.P., Huo, G.P., and Han, B.: Mineral
1028 exploration using CSAMT data: application to Longmen region metallogenic belt,
1029 Guangdong Province, China, *Geophysics*, 78, B111–B119, 2013.
1030 <https://doi.org/10.1190/geo2012-0115.1>.
- 1031 41. Ingebritsen, S.E., and Manning, C.E.: Permeability of the continental crust: dynamic
1032 variations inferred from seismicity and metamorphism, *Geofluids*, 10, 193–205, 2010.
1033 <https://doi.org/10.1111/j.1468-8123.2010.00278.x>.
- 1034 42. ISRM.: Suggested methods for rock characterization, testing and monitoring: 2007–2014,
1035 Springer, 2015. <https://doi.org/10.1007/978-3-319-07713-0>.
- 1036 43. Jardani, A., Revil, A., Santos, F., Fauchard, C., and Dupont, J.P.: Detection of
1037 preferential infiltration pathways in sinkholes using joint inversion of self - potential and

1038 EM - 34 conductivity data, *Geophysical Prospecting*, 55(5), 749–760, 2007.
1039 <https://doi.org/10.1111/j.1365-2478.2007.00638.x>.

1040 44. Jasechko, S., Seybold, H., Perrone, D., Fan, Y., Shamsudduha, M., Taylor, R.G., Fallatah,
1041 O., and Kirchner, J.W.: Rapid groundwater decline and some cases of recovery in
1042 aquifers globally, *Nature*, 625, 715–721, 2024. [https://doi.org/10.1038/s41586-023-](https://doi.org/10.1038/s41586-023-06879-8)
1043 [06879-8](https://doi.org/10.1038/s41586-023-06879-8).

1044 45. Jiang, X.W., Wan, L., Wang, J.Z., Yin, B.X., Fu, W.X., and Lin, C.H.: Field
1045 identification of groundwater flow systems and hydraulic traps in drainage basins using a
1046 geophysical method, *Geophysical Research Letters*, 41(8), 2812–2819, 2014.
1047 <https://doi.org/10.1002/2014GL059579>.

1048 46. Kouadio, K.L., Liu, R., Malory, A.O., and Liu, C.: A novel approach for water reservoir
1049 mapping using controlled source audio-frequency magnetotelluric in Xingning area,
1050 Hunan Province, China, *Geophysical Prospecting*, 71, 1708–1727, 2023.
1051 <https://doi.org/10.1111/1365-2478.13385>.

1052 47. Laghari, A.N., Vanham, D., and Rauch, W.: The Indus basin in the framework of current
1053 and future water resources management, *Hydrology and Earth System Sciences*, 16 (4),
1054 1063–1083, 2012. <https://doi.org/10.5194/hess-16-1063-2012>.

1055 48. Majumdar, R.K., and Das, D.: Hydrological characterization and estimation of aquifer
1056 properties from electrical sounding data in Sagar Island region, South 24 Parganas, West
1057 Bengal, India, *Asian J Earth Sci*, 4, 60–74, 2011.
1058 <http://dx.doi.org/10.3923/ajes.2011.60.74>.

- 1059 49. Manning, C.E., and Ingebritsen, S.E.: Permeability of the continental crust: Implications
1060 of geothermal data and metamorphic systems, *Reviews of Geophysics*, 37(1), 127–150,
1061 1999. <https://doi.org/10.1029/1998RG900002>.
- 1062 50. Mira Geoscience Ltd.: GOCAD Mining Suite 3D Geological Modeling Software. Nancy
1063 University, Lorraine, France, 1999.
- 1064 51. Mudunuru, M.K., Cromwell, E.L.D., Wang, H., and Chen, X.: Deep learning to estimate
1065 permeability using geophysical data, *Advances in Water Resources*, 167, 104272, 2022.
1066 <https://doi.org/10.1016/j.advwatres.2022.104272>.
- 1067 52. Niwas, S., and De Lima, O.A.L.: Aquifer parameter estimation from surface resistivity
1068 data, *Groundwater*, 41, 94–99, 2003. <https://doi.org/10.1111/j.1745-6584.2003.tb02572.x>.
- 1069 53. Nwosu, L.I., Nwankwo, C.N., and Ekine, A.S.: Geoelectric investigation of the hydraulic
1070 properties of the aquiferous zones for evaluation of groundwater potentials in the
1071 complex geological area of imostate, Nigeria, *Asian J Earth Sci*, 6, 1–15, 2013.
1072 <https://scialert.net/abstract/?doi=ajes.2013.1.15>.
- 1073 54. Pellet, H., Arfib, B., Henry, P., Tournon, S., and Gassier, G.: Mesoscale permeability
1074 variations estimated from natural airflows in the decorated Cosquer Cave (southeastern
1075 France), *Hydrol. Earth Syst. Sci.*, 28, 4035–4057, 2024. [https://doi.org/10.5194/hess-28-](https://doi.org/10.5194/hess-28-4035-2024)
1076 [4035-2024](https://doi.org/10.5194/hess-28-4035-2024).
- 1077 55. Phoenix Geophysics CMTPro, The Canadian Phoenix CMT Pro Version software for
1078 CSAMT data processing. Toronto, Ontario, Canada, 2020.
- 1079 56. Phoenix Geophysics CSAMT-SW, The Canadian Phoenix CSAMT-SW Version software
1080 for CSAMT data inversion. Toronto, Ontario, Canada, 2020.

- 1081 57. Pollock, D., and Cirpka, O.A.: Fully coupled hydrogeophysical inversion of a laboratory
1082 salt tracer experiment monitored by electrical resistivity tomography, *Water Resources*
1083 *Research*, 48(1), W01505, 2012. <https://doi.org/10.1029/2011WR010779>.
- 1084 58. Qin, X.: Application of Unwedge program to geological stability analysis of deep buried
1085 deposits, *Comprehensive*, 8, 270–273, 2017 (In Chinese).
- 1086 59. Revil, A., and Cathles III, L.M.: Permeability of shaly sands, *Water Resources Research*,
1087 35(3), 651–662, 1999. <https://doi.org/10.1029/98WR02700>.
- 1088 60. Rodi, W., and Mackie, R.L.: Nonlinear conjugate gradients algorithm for 2-D
1089 magnetotelluric inversion, *Geophysics*, 66 (1), 174–187, 2001.
1090 <https://doi.org/10.1190/1.1444893>.
- 1091 61. Saar, M.O., and Manga, M.: Depth dependence of permeability in the Oregon Cascades
1092 inferred from hydrogeologic, thermal, seismic, and magmatic modeling constraints,
1093 *Journal of Geophysical Research*, 109(B4), B04204, 2004.
1094 <https://doi.org/10.1029/2003JB002855>
- 1095 62. Simpson, F., and Bahr, K.: *Practical magnetotellurics*. Cambridge University Press,
1096 Cambridge. 254 pp, 2005. <https://doi.org/10.1017/CBO9780511614095>.
- 1097 63. Singh, K.P.: Nonlinear estimation of aquifer parameters from surficial resistivity
1098 measurements, *Hydrology and Earth System Sciences Discussions*, 2 (3), 917–938, 2005.
1099 <https://doi.org/10.5194/hessd-2-917-2005>.
- 1100 64. Smith, J.T., and Booker, J.R.: Rapid inversion of two-and three-dimensional
1101 magnetotelluric data, *Journal of Geophysical Research: Solid Earth*, 96 (B3), 3905–3922,
1102 1991. <https://doi.org/10.1029/90JB02416>.

- 1103 65. Soupios, P.M., Kouli, M., Vallianatos, F., Vafidis, A., and Stavroulakis, G.: Estimation of
1104 aquifer hydraulic parameters from surficial geophysical methods: a case study of Keritis
1105 Basin in Chania (Crete–Greece), *J Hydrol*, 1, 122–131, 2007.
1106 <https://doi.org/10.1016/j.jhydrol.2007.02.028>.
- 1107 66. Wada, Y., Van Beek, L.P., Van Kempen, C.M., Reckman, J.W., Vasak, S., and Bierkens,
1108 M.F.: Global depletion of groundwater resources, *Geophysical Research Letters*, 37 (20),
1109 L20402, 2010. <https://doi.org/10.1029/2010GL044571>.
- 1110 67. Wang, R., Yin, C., Wang, M., and Di, Q.: Laterally constrained inversion for CSAMT
1111 data interpretation, *Journal of Applied Geophysics*, 121, 63–70, 2015.
1112 <https://doi.org/10.1016/j.jappgeo.2015.07.009>.
- 1113 68. Waxman, M.H., and Smits, L.J.M.: Electrical conductivities in oil-bearing shaly sands,
1114 *Society of Petroleum Engineers Journal*, 8(02), 107–122, 1968.
1115 <https://doi.org/10.2118/1863-A>.
- 1116 69. Webring, M.W.: MINC: A Gridding Program Based on Minimum Curvature: U.S.
1117 Geological Survey Open File Report, 81–1224, p. 41p, 1981.
1118 <https://doi.org/10.3133/ofr811224>.
- 1119 70. Worthington, S.R.H., Davies, G.J., and Alexander, E.C. Jr.: Enhancement of bedrock
1120 permeability by weathering, *Earth-Sci Rev*, 160, 188–202, 2016.
1121 <https://doi.org/10.1016/j.earscirev.2016.07.002>.
- 1122 71. Yan, Y., Ma, L., Qian, J., Zhao, G., Fang, Y., Ma, H., and Wang, J.: Estimating
1123 permeability of rock fracture based on geometrical aperture using geoelectrical
1124 monitoring, *Journal of Hydrology*, 644, 132067, 2024.
1125 <https://doi.org/10.1016/j.jhydrol.2024.132067>.

- 1126 72. Yang, J., Zhang, H., and Cui, Z.: Stability Analysis and Countermeasures of Rock Block
1127 in Underground Cavern, *Guangdong Water Resources and Hydropower* 5, 23–27, 2021
1128 (In Chinese)
- 1129 73. Zhang, M., Farquharson, C.G., and Liu, C.: Improved controlled source audio-frequency
1130 magnetotelluric method apparent resistivity pseudo-sections based on the frequency and
1131 frequency–spatial gradients of electromagnetic fields, *Geophysical Prospecting*, 69, 474–
1132 490, 2021. <https://doi.org/10.1111/1365-2478.13059>.
- 1133 74. Zhu, L., Gong, H., Dai, Z., Guo, G., and Teatini, P.: Modeling 3-D permeability
1134 distribution in alluvial fans using facies architecture and geophysical acquisitions, *Hydrol.*
1135 *Earth Syst. Sci.*, 21, 721–733, 2017. <https://doi.org/10.5194/hess-21-721-2017>.
- 1136 75. Zonge, K.L., and Hughes, L.J.: Kenneth L. Zonge and Larry J. Hughes, (1991), "9.
1137 Controlled Source Audio-Frequency Magnetotellurics," *Investigations in Geophysics*,
1138 713–810, 1991. <https://doi.org/10.1190/1.9781560802686.ch9>.